Whole-Brain Cell-Cell Interaction Axes Explaining Tissue Vulnerability Across the Neurodegenerative Spectrum

Authors: Veronika Pak[1-3], Joon Hwan Hong[1-3], Tobias R. Baumeister[1-3], Gleb Bezgin[1-4], Corina Nagy[3,5-6], Simon Ducharme[5-6], Mahsa Dadar[5-6], Yashar Zeighami[5-6], Yasser Iturria-Medina[1-4*].

Affiliations:

[1] Department of Neurology and Neurosurgery, McGill University, Montreal, Quebec, Canada
[2] McConnell Brain Imaging Centre, Montreal Neurological Institute, Montreal, Quebec, Canada
[3] Ludmer Centre for Neuroinformatics & Mental Health, Montreal, Quebec, Canada
[4] McGill Centre for Studies in Aging, Montreal Quebec, Canada
[5] Department of Psychiatry, McGill University, Montreal, Quebec, Canada
[6] The Douglas Research Center, Montreal, Quebec, Canada
* Correspondence to: YIM (yasser.iturriamedina@mcgill.ca).

Abstract

Cell-cell communication is essential for proper brain functioning and health. Here, we characterize whole-brain patterns of cellular interactions that spatially align with tissue damage across 13 neurodegenerative conditions, including early- and late-onset Alzheimer's disease (EOAD, LOAD), presenilin-1 mutations (PS1), frontotemporal lobar degeneration, Parkinson's disease (PD), dementia with Lewy bodies (DLB), and amyotrophic lateral sclerosis (ALS). By integrating spatial gene expression with structural MRI data, we created over 1,000 whole-brain maps of ligand-receptor interactions. Multivariate analysis revealed three principal axes of cell-cell communication underlying brain tissue vulnerability. The first axis involved neuron-astrocyte-microglia interactions, explaining atrophy patterns shared by frontotemporal lobar degeneration and Alzheimer's disease subtypes. Moreover, the first axis was enriched with genes involved in regulation or spreading of Aβ/tau and/or Alzheimer's disease risk. Two complementary axes involving neurons, endothelial cells, and astrocytes explained patterns specific to PS1 and PD. Notably, we confirmed that cell-cell interactions identified for LOAD were also associated with frontal cortex atrophy in 375 participants from an independent database. These findings reveal both distinctive and shared molecular signaling pathways underlying tissue vulnerability across neurodegenerative disorders, clarifying disease mechanisms and highlighting potential cellular targets for therapeutic interventions.

INTRODUCTION

A fundamental question in neuroscience concerns how distinct brain cell populations contribute to neurodegenerative disease pathogenesis [1,2]. While traditionally viewed through a neuron-centric lens [3], compelling evidence now indicates that non-neuronal cells serve as critical drivers of neurodegeneration [1,4-7]. Advanced multi-omics investigations have reinforced the essential role these cells play in neurodegenerative processes [8-10]. Cell-cell communication represents a particularly important focus, as its precise regulation underpins the nervous system's equilibrium and health [11]. For instance, dysfunctions in signalling between neurons and glial cells, including microglia, astrocytes, and oligodendrocytes, are thought to lead to inflammation, impaired glutamate metabolism, demyelination, and consequent neuronal death [12-14]. Characterizing how these cellular interactions modulate vulnerability to diverse neurodegenerative conditions is essential for advancing our mechanistic understanding and for the development of novel therapies.

Significant advances in multi-omics, particularly single-cell and single-nucleus RNA sequencing (snRNA-seq) combined with spatial transcriptomics, have enabled studying cell-cell communication in health and disease [15,16]. Despite these advances, detecting global patterns in cell communication across the entire human brain is still challenging, as these methods are often limited to isolated regions of interest. In the context of neurodegeneration, understanding whole-brain patterns is essential since the clinical manifestations of different conditions vary greatly depending on the specific anatomical/functional pathways affected [17]. Therefore, the limited tissue coverage provided by these methods constrains the ability to conduct systematic analyses across different brain regions and tissue damage patterns specific to different diseases.

In this study, we characterize whole-brain patterns of neurotypical cell-cell interactions spatially aligned with tissue damage observed in 13 neurodegenerative conditions, including early- and late-onset AD (EOAD and LOAD), genetic mutations in presenilin-1 (PS1 or PSEN1), Parkinson's disease (PD), dementia with Lewy bodies (DLB), amyotrophic lateral sclerosis (ALS), and both clinical and pathological subtypes of frontotemporal lobar degeneration (FTLD) [18-21]. First, we generate whole-brain cell-type-specific maps of ligand-receptor interactions derived from literature-curated databases, using spatial gene expression and magnetic resonance imaging (MRI) data. Next, using multivariate statistical approaches, we identify principal axes of cell-cell interactions underlying spatial vulnerability patterns across the 13 neurodegenerative conditions. We proceed to use an independent LOAD dataset (N=375) with matched brain RNA and atrophy evaluations to validate the key interactions identified with our *in-silico* approach, confirming the generalizability of our findings. Finally, we conduct gene enrichment analyses on key cell-cell interactions from the prominent axes to uncover underlying signalling pathways predisposing atrophy across the neurodegeneration. This study represents a significant advancement in our understanding of neurodegenerative diseases, with potential implications for the development of targeted therapeutics that modulate specific cell-cell interactions. Notably, by

identifying the cellular communication networks that underlie regional vulnerability, we provide a novel framework for understanding why certain brain regions are primarily targeted by specific neurodegenerative conditions.

RESULTS

Reconstructing brain maps of cell-cell interactions

In a first of its kind analysis, we reconstructed whole-brain maps of molecular interactions across six major cell types of the neurotypical human brain (see Fig. 1), including excitatory and inhibitory neurons, astrocytes, microglia, endothelial cells, oligodendrocytes, and oligodendrocyte precursor cells (OPCs). First, we utilized bulk microarray gene expression data from six human donors from the Allen Human Brain Atlas (AHBA) [22,23]. Next, we integrated 10 curated databases that included literature-supported ligand-receptor (LR) or molecular interaction pairs specific to humans [24,25] (see *Methods, Ligand-receptor interaction databases*). From the overlap of these 10 databases with the ~20,000 genes available in the AHBA, we identified 1,037 pairs whose ligands and receptors were previously found to be expressed in the six studied cell types. For a pair to be selected, both the ligand and receptor (or molecule) had to be annotated as being expressed in one of the targeted cell types, with agreement from at least two out of five public gene marker databases (Fig. 1b; see *Methods, Cell type annotation*). The databases included CellMarker 2.0 [26], PanglaoDB [27], BRETIGEA [28], and the immunohistochemistry and single cell databases from the Human Protein Atlas [29].

The distribution of the different types of annotated cell-cell communication is visualized in Figure 1c. The majority of interactions involved neuron-neuron and neuron-endothelial communication, covering 276 and 143 interacting pairs, respectively. The full list of 1,037 interacting pairs and their cell type annotation are listed in the **Supplementary Table 1**. To quantify brain-wide cell-cell communication for each of the pairs within each voxel of the brain defined by the MNI-152 space [30], we calculated the product of ligand and receptor expression levels within each voxel (Fig.1d; see *Methods, Reconstruction of interaction maps*). Out of 1,027 available for validation pairs, 409 (39.82%) of AHBA-derived interactions significantly correlated with interactions derived from snRNA-seq data across several regions in healthy human brains (see more details in “Comparison with interactions derived from single nucleus data”). Notice that although most interactions included in our analyses represent direct extracellular LR communications, some pairs involved molecules that either do not interact directly, function in roles other than canonical LR signalling, or participate in intracellular processes. For example, the interaction between FZD8 and LRP6 involves a receptor complex involved in Wnt signalling initiation rather than a typical LR pairing[31]. SV2A/B/C are extracellular synaptic glycoprotein vesicles[32]. The presenilin protein (PS) functions as part of the

γ-complex rather than as a ligand[33]. GNAI2 (guanine nucleotide-binding protein subunit alpha i2) frequently appears as a ligand in the LR databases such as CellTalkDB[34], but acts as a G-protein subunit mediating intracellular signal transduction downstream of receptor activation[35].

Next, to uncover spatial associations between the interaction maps and the atrophy patterns observed in 13 neurodegenerative conditions, we performed partial least squares (PLS) analysis with cross-correlation, using voxels as observations (Fig. 1e), and interactions and disorders as predictor and response variables, respectively. Atrophy maps for the following neurodegenerative conditions were included: early- and late-onset Alzheimer's disease (EOAD and LOAD, respectively), Parkinson's disease (PD), amyotrophic lateral sclerosis (ALS), dementia with Lewy bodies (DLB), mutations in presenilin-1 (PS1), clinical variants of FTD (the behavioral variant [bvFTD] and the non-fluent and semantic variants of primary progressive aphasia [nfvPPA and svPPA]), and FTLD-related pathologies such as FLTD-TDP (TAR DNA-binding protein) types A and C, three-repeat tauopathy and four-repeat tauopathy (3RTau and 4RTau) [18-21]. The latent variables (hereby axes) identified by PLS, along with their contributing weights, were subsequently analyzed in downstream analyses. In sum, this approach identified the specific molecular interactions and neurodegenerative conditions that contributed most to the covariance between cell-cell communication and tissue atrophy, reflecting potential vulnerabilities.

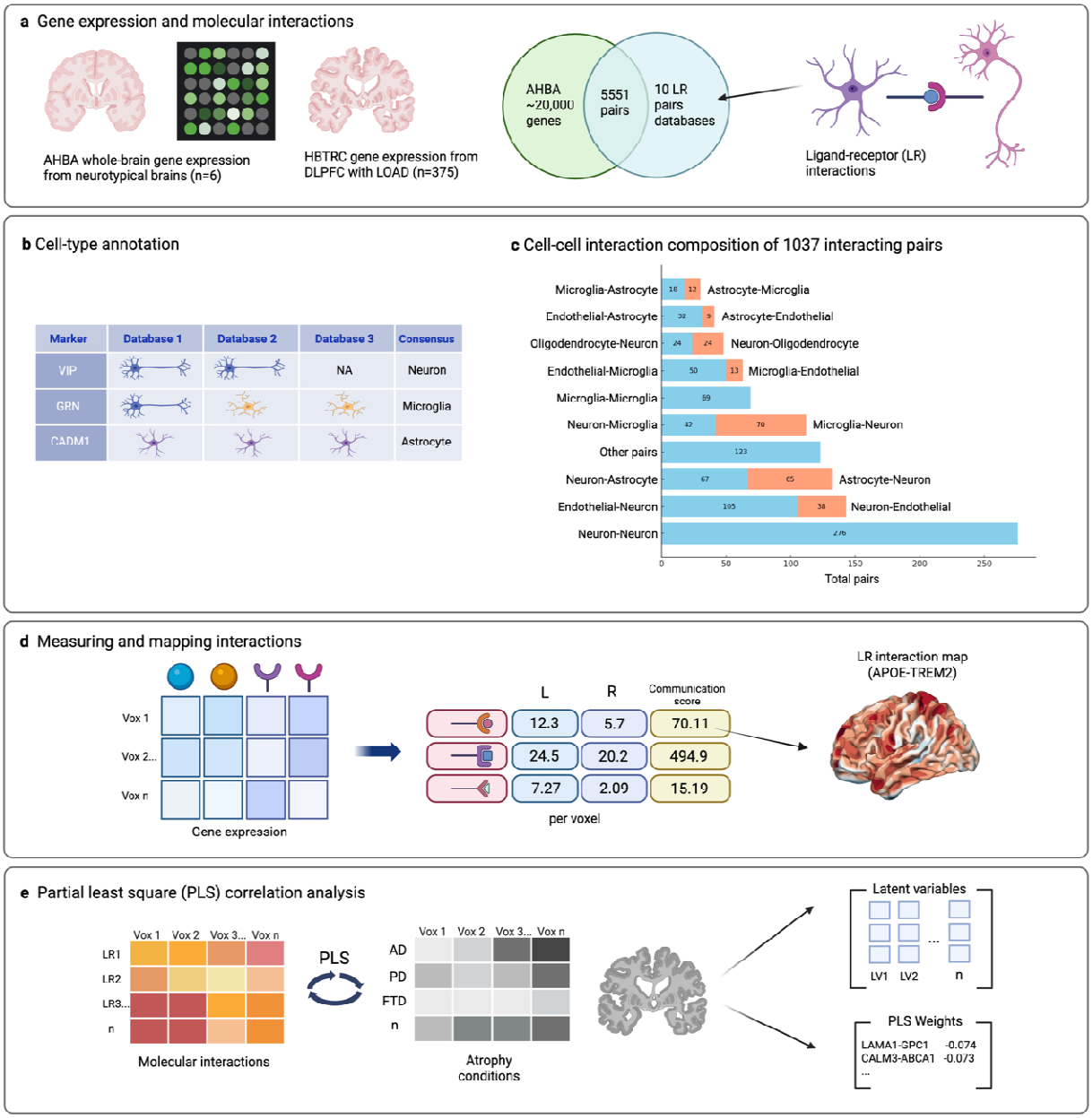

Figure 1 | Diagram illustrating the process of generating molecular interaction maps and analyzing their relationship with atrophy in neurodegeneration. **a)** Interpolated whole-brain RNA expression from healthy individuals (Allen Human Brain Atlas; AHBA) and dorsolateral prefrontal cortex (DLPFC) expression from LOAD patients (Harvard Brain Tissue Resource Centre; HBTRC) were analyzed. Interaction pairs from 10 curated human-specific databases (blue circle) were cross-referenced with ~20,000 genes from the AHBA (green circle). **b**) The R package BrainCellAnn was used to annotate marker genes associated with interacting pairs. Only pairs whose ligand and receptor genes were annotated as a cell type of interest by at least two marker databases were included in the analysis, resulting in 1,037 pairs. **c**) Breakdown of the annotated cell-cell interaction ratios, split by direction of interaction types. **d**) The product of ligand and receptor (or molecule 1 and molecule 2) expression levels within each MNI template voxel (1.5 x 1.5 x 1.5 mm^3 size) was calculated to generate a whole-brain interaction map for each LR pair. **e**) PLS

correlation was performed at the voxel level, with the 1,037 interaction maps as predictors and atrophy maps for 13 neurodegenerative conditions as outcomes.

Obtained maps of dopamine signalling interactions reflect major dopaminergic pathways

To validate our approach for reconstructing cell-cell interaction maps, we proceeded to test whether the inferred dopamine-related interactions were particularly enriched in key regions of major dopaminergic pathways (e.g., substantia nigra and nucleus accumbens). We generated eight maps of known interactions, including dopamine receptor families (DRD 1-5) and interactions involving the solute carrier family 18-member 2 (*SLC18A2*). SLC18A2 is essential for enabling the release of neurotransmitters, such as dopamine, norepinephrine, serotonin, and histamine, via synaptic vesicles into the synaptic cleft [36]. We extracted regional values from the maps defined by the extended Desikan-Killiany-Tourville (DKT) atlas [37,38], with manually added subcortical regions. **Figure 2** depicts a heatmap of the regional communication values, which were scaled relative to each other for each interaction.

We verified (Fig. 2) that subcortical regions associated with dopamine pathways were enriched with interactions involving GNAI2-DRD3, GNAI2-DRD2, and SLC18A2, compared to other brain regions. Specifically, SLC18A2-related interactions were particularly enriched in the basal forebrain, thalamus, red nucleus, and substantia nigra—regions that play a key role in dopaminergic, cholinergic, and glutamatergic neurotransmission, supporting motor and cognitive functions. Furthermore, interactions involving DRD2 and DRD3 receptors were prominent in striatum regions, including the putamen, caudate, and nucleus accumbens. All three regions receive dopaminergic projections from the ventral tegmental area and the substantia nigra. GNAI2-DRD2 interactions were particularly enriched across all regions heavily involved in the dopamine pathways. In contrast, interactions involving DRD1, DRD4, and DRD5 receptors were not specifically enriched in regions associated with dopamine pathways.

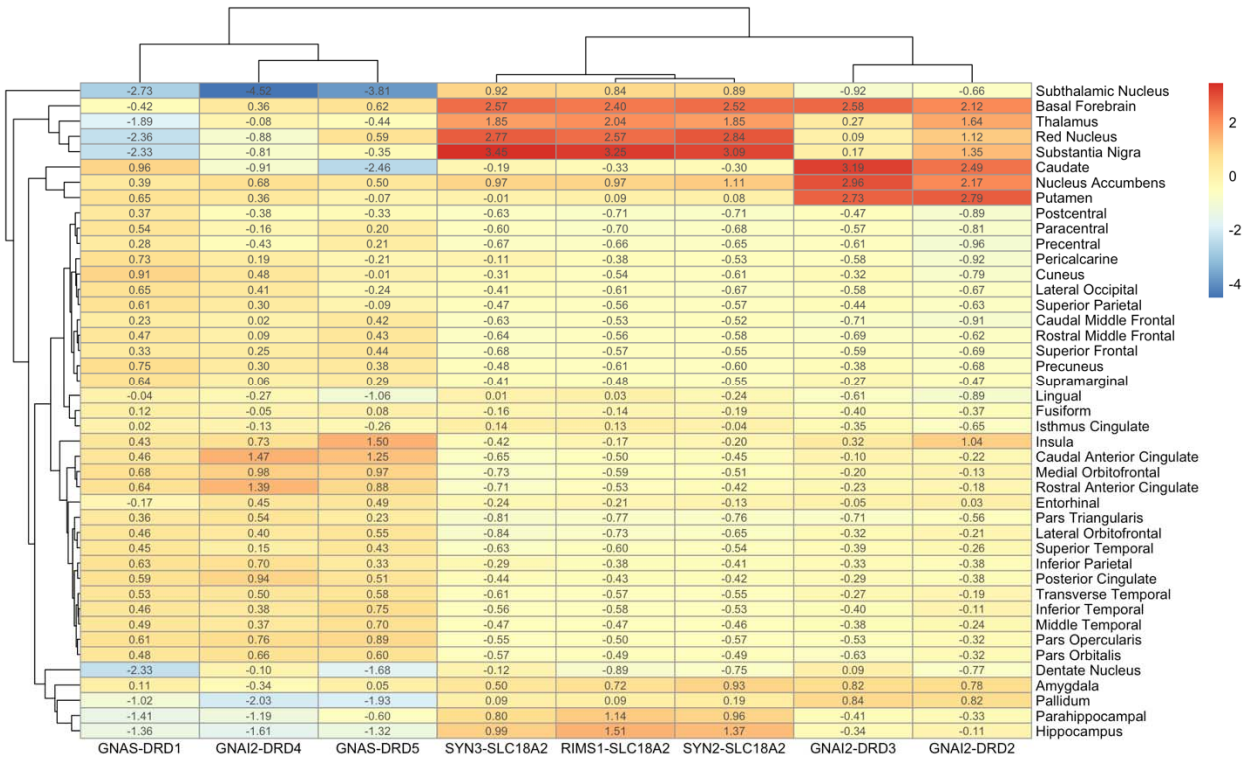

Figure 2 | Regional communication values for dopamine-related interactions. Regions were defined by the extended DKT atlas, with additional subcortical areas included. For each interaction, regional values were normalized, with higher positive scores (in red) indicating stronger communication relative to other regions, and lower negative scores (in blue) representing weaker communication. Regions involved in dopaminergic pathways such as the basal forebrain grouped together and showed higher communication scores for GNAI2-DRD2, GNAI2-DRD3, and SLC18A2 interactions.

First axis of LR interactions predominantly captures tissue damage in FTLD and AD

We applied multivariate PLS correlation and permutation tests to explore the spatial covariation between 1,037 interaction pairs and atrophy patterns across 13 neurodegenerative conditions. All 13 latent variables (LVs) or axes of covariation were significant (all $p < 0.05$, corrected via randomized permutations), possibly due to a large number of observations (~300,000 voxels). A thousand permutation and bootstrap iterations were performed to estimate statistical significance and reliability (see *Methods*, *Partial least square analysis*). Results for the first three axes are summarized in the **Supplementary Table 2**.

The first axis (latent variable 1) explained 84.27% of the covariance between interactions and atrophy patterns. Figure 3a presents the top 5% of LR pairs with the biggest contributions measured by PLS weights in explaining atrophy. Among these, the COL1A1-CD36 interaction and other CD36-associated pairs in the top 10 contributed most to explaining atrophy patterns

(Fig. 3a). CD36, also known as platelet glycoprotein 4 fatty acid translocase, is a membrane glycoprotein that binds Aβ as a scavenger receptor. It has been linked to neurodegeneration through its role in Aβ clearance, and its increased activity may lead to oxidative stress, neurovascular dysfunction, and chronic inflammation in AD [39-41]. When CD36 interacts with Toll-like receptors TLR4 and TLR6, forming signaling complexes (e.g., CD36-TLR4 and CD36-TLR6 from the top 15 pairs contributing to the first axis), it amplifies inflammatory responses in the brain when activated by fibrillary Aβ peptides [42]. Three CD36 interactions in the top 12 pairs involved thrombospondin (THBS), which showed protective effects against Aβ-induced mitochondrial dysfunction [43] and Aβ-mediated synaptic pathology in AD [44].

The top 10% (104 interactions) from the first axis included other prominent interactions, which have been already recognized as potential therapeutic targets for neurodegenerative diseases, including FGF9-FGFR3, APOC1-APP, HSP90B1-ERBB2, APOE-GPC4, APOE-APP, and others [45-49]. For example, overexpression of fibroblast growth factor 9 (FGF9) has been shown to induce myelin loss and gray matter neuroaxonal atrophy in multiple sclerosis (MS) [49]. Its complementary receptor, fibroblast growth factor receptor 3 (FGFR3), has been recently found to mediate Aβ-induced tau uptake and facilitate neuroprotective neuron-microglia communication in AD [50,51]. Another notable pair is APOE-GPC4, which involves apolipoprotein E (APOE), the major genetic risk factor for AD, and glypican-4 (GPC4), an astrocyte-secreted protein. GPC4 secreted by astrocytes binds to APOE4 to drive tau hyperphosphorylation, a critical process in pathogenesis of many dementia conditions [47]. As for a similar AD risk gene, apolipoprotein C1 (APOC1) can enhance the cleavage of amyloid precursor protein (APP), thereby increasing the production and accumulation of Aβ, and it can also supress inflammatory responses in the brain produced by microglia and astrocytes [52,53]. Heat shock protein 90 beta 1 (HSP90B1), which is dysregulated in AD brains, has been linked to astrogliosis and tau-driven neurotoxicity [54-56], while heat shock proteins more broadly may also contribute to resilience against AD [57] . Lastly, interactions with serotonin binding receptor, such as 5-hydroxytryptamine receptor 2C (HTR2C)**,** and laminin subunit alpha 1 (LAMA1) showed prominent contributions.

Figure 3b shows bar graphs representing the atrophy conditions ranked by their contributions to the first axis, with five FTLD-related conditions showing the largest weights, followed by EOAD and LOAD. This suggests that the identified cell-cell interactions mostly explain the atrophy patterns common to the FTLD conditions. Spatial atrophy associated with 4-repeat tauopathy and 3-repeat tauopathy demonstrated the highest contributions, followed by TDP-43 proteinopathy types A and C, and svPPA.

When interpreting these results, a positive association, where both condition and interaction weights are positive, suggests that regions with stronger communication between certain molecules (e.g., COL1A1-CD36) are more vulnerable to developing the atrophy patterns seen in these conditions (FTLD subtypes). On the other hand, reduced interactions between genes with negative PLS weights such as LGI2-ADAM22/11 and FGF9-FGFR3/FLRT1 predispose to

atrophy in the same conditions, suggesting potential protective effect. Figure 3c displays surface plots (lateral views of the left hemisphere) illustrating the atrophy map for 4RTau alongside the interaction map for COL1A1-CD36. The partial spatial alignment between these maps suggests that certain brain tissues with enhanced communication between COL1A1 and CD36 could be susceptible to develop atrophy specific to 4RTau.

Among the top 10% of pairs, 28 of 104 showed strong bi-directional interaction between astrocytes and neurons, along with prominent contributions from neuron-microglia (13) and neuron-neuron pairs (24) (Fig. 3d). Overall, interactions involving both microglia (9) and astrocytes (9) were predominant in the first axis (see microglia-microglia, astrocyte-astrocyte, and microglia-endothelial), compared to endothelial-related interactions.

PANTHER database was used for gene enrichment since its collection of biological pathways is specific for cell signalling [58]. The top interacting molecules from the top 10% were significantly enriched for pathways including Slit/Robo-mediated axon guidance, Notch signalling, integrin signalling, and Alzheimer's disease presenilin pathway (Fig.3e; $p < 0.001$, FDR-corrected). Growing body of research has demonstrated that Slit/Robo signaling regulates such processes as angiogenesis and inflammatory cell chemotaxis, which are implicated in neurodegeneration [59]. Notch signaling has been long associated with multiple neurodegenerative disorders such as AD, MS, ALS, and neurovascular aging by affecting multiple cellular processes [60,61]. Integrin signaling also plays a critical role in neurodegeneration, as integrins are cell adhesion molecules that maintain synaptic and axonal integrity and also mediate the response of immune cells, such as microglia and astrocytes, to brain injury or degeneration by enhancing inflammatory signaling [62].

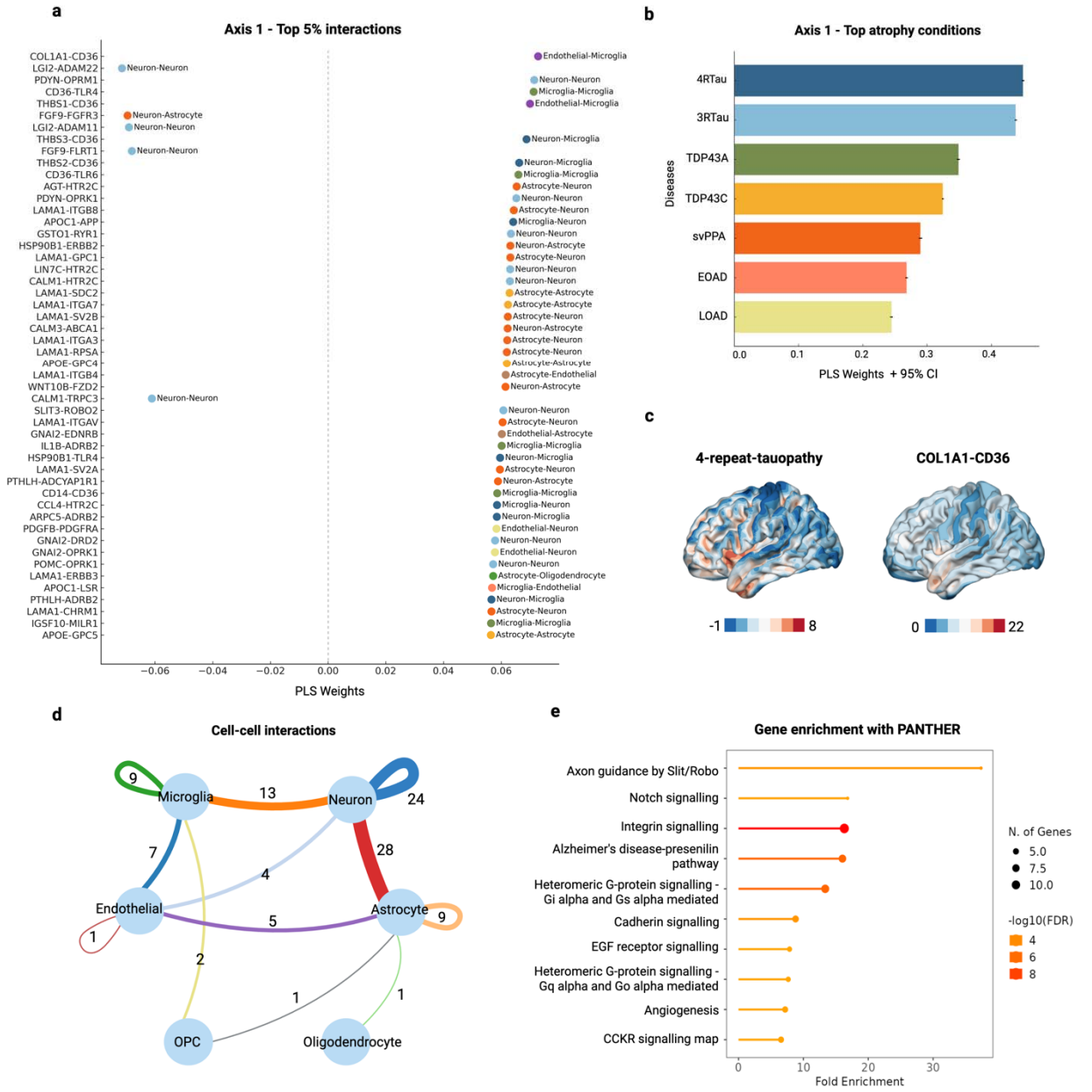

Figure 3 | Top ligand-receptor interactions and neurodegenerative conditions contributing to the first axis. **a**) The top 5% of pairs with the largest contributions to spatial covariance with atrophy are colored by annotated interaction type. The interaction COL1A1-CD36 showed the highest contribution (0.073). PLS weights reflect relative contributions to the axes and are not interpretable as effect sizes or percentages. **b**) Top neurodegenerative conditions contributing to the first axis, with FTLD-related conditions (4RTau, 3RTau, TDP43A & C, svPPA) making the largest contributions (error bars defined by 95% CI). **c**) Surface plots (lateral views of the left hemisphere) displaying the atrophy map for 4RTau and the LR interaction map for COL1A1-CD36. Color bars indicate the strength of cell-cell communication and tissue loss, with negative values indicating tissue enlargement relative to healthy controls. **d**) Network visualization of cell-cell interactions counts from the top 10% annotated pairs, highlighting strong bi-directional signaling between neurons and astrocytes, neurons between each other, and neurons and

microglia. Numbers on edges indicate counts of unique interactions. Cell types for interaction types were annotated using five gene marker databases. **e**) Gene enrichment analysis using the PANTHER database, indicated significant enrichment of pathways related to Slit/Robo-mediated axon guidance, Notch signalling, integrin signalling, and Alzheimer's disease presenilin ($p < 0.001$ FDR corrected).

Second axis of cell-cell interactions explains tissue damage in PS1 and DLB

The second axis explained 7.61% of the covariance between interactions and atrophy patterns. Figure 4a shows the PLS weights for the top 5% of interacting pairs contributing to the second axis, with interactions such as FAM3C-GLRA2 (family with sequence similarity 3 and glycine receptor alpha 2) and LGI-related (leucine-rich glioma inactivated) interactions showing the largest contributions to explaining atrophy. The neurodegenerative conditions with positive weights (Fig. 4b) were PS1 mutation-related dementia (associated with EOAD), atrophy patterns in EOAD itself, and ALS. These results suggest that the atrophy patterns common to these three conditions were mostly explained by increased communication between LGI-related interactions, such as LGI3-ADAM22 and LGI2-ADAM23, and decreased interactions between pairs like FAM3C and GLRA2.

Figure 4c displays the surface plots of the atrophy map for PS1 mutation carriers and the interaction map for FAM3C-GLRA2, highlighting their negative association in strength patterns. Genetic mutations in amyloid precursor protein (APP), such as PS1, modify Aβ biosynthesis and cause an autosomal dominant form of AD [63]. Like PS1, FAM3C is a γ-secretase complex-binding protein. Previous studies have shown that FAM3C expression declines with aging and promotes Aβ accumulation in AD through its interaction with presenilin, with reduced FAM3C levels linked to the onset of sporadic AD, highlighting it as a potential therapeutic target [64,65]. Our results further support this association, as decreased FAM3C-GLRA2 communication indicates vulnerabilities to atrophy in PS1 mutation-related dementia and EOAD. Similarly, increased communication in FAM3C-GLRA2 and SLIT3-ROBO, along with decreased LGI-related interactions, were associated with the atrophy patterns common to DLB, TDP43 proteinopathy type C, and PD.

The interaction counts from the top 10% of pairs with the highest PLS weights captured a strong influence from neuron-neuron interactions (37), along with significant contributions from neuron-endothelial (18) and neuron-astrocyte (15) bidirectional interactions, as shown in Figure 4d. Unlike in the first axis, interactions involving neurons and oligodendrocytes, as well as neurons and endothelial cells, were more prominently represented in the second axis. For example, the LGI3 ligand, which showed multiple high contributions, is known to be uniquely secreted from oligodendrocytes in the brain and is involved in neuron-glial interaction processes, such as myelination [66].

Gene enrichment analysis using the PANTHER database (Fig. 4e) indicated significant enrichment of pathways related to Slit/Robo-mediated axon guidance, enkephalin release, integrin signaling, and blood coagulation. Elevated enkephalin levels have been previously linked to Aβ-dependent alterations and cognitive dysfunction in both AD human brains and mouse models of AD [67]. The presence of blood coagulation supports the critical role of endothelial interactions in the second axis.

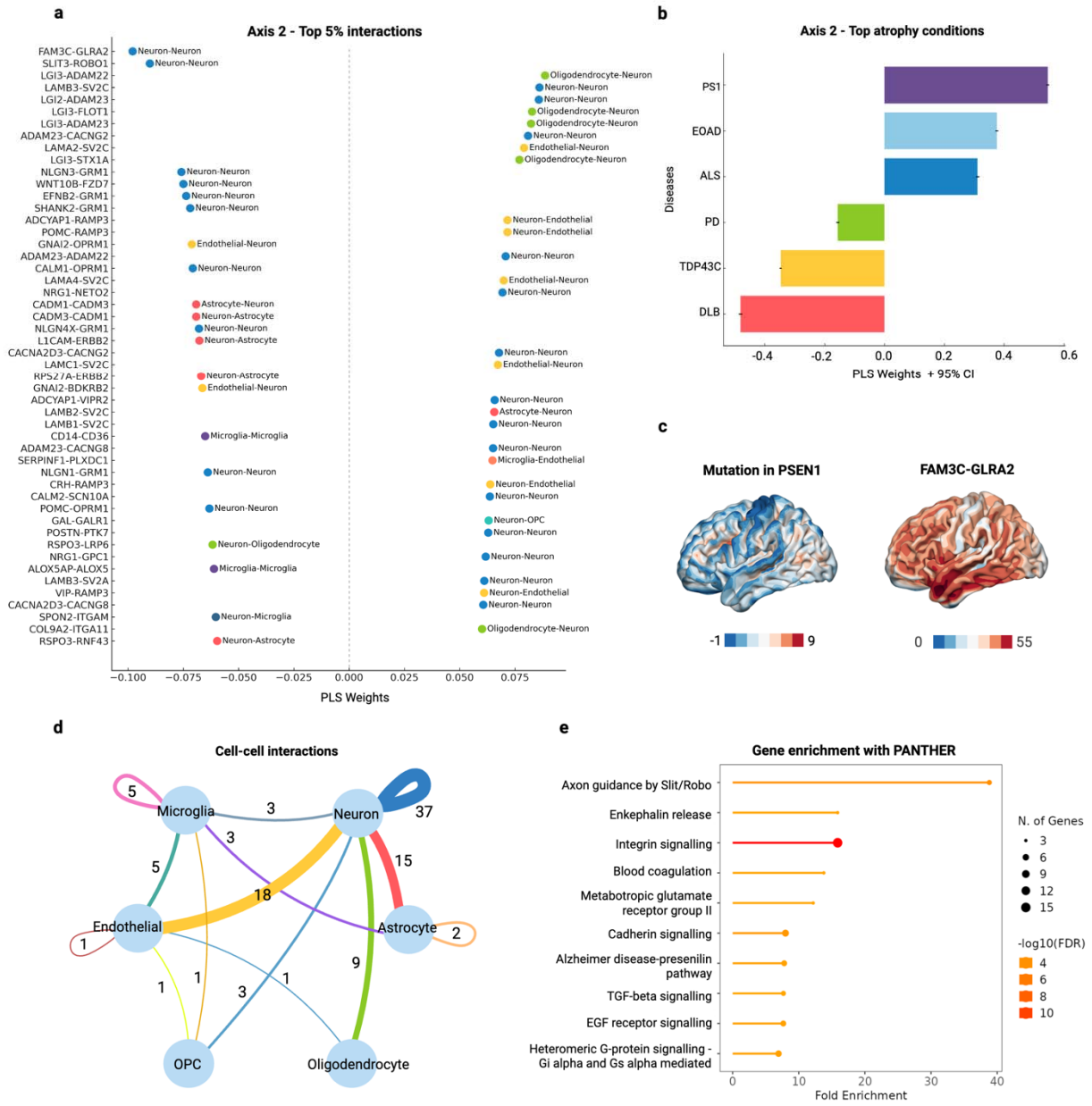

Figure 4 | Top ligand-receptor interactions and neurodegenerative conditions contributing to the second axis. **a**) PLS weights for the top 5% contributing interactions, colored by annotated cell-cell communication type. FAM3C-GLRA2 showed the highest contributions with negative weights. **b**) Top neurodegenerative conditions with atrophy patterns contributing to the second axis. Mutation in PS1 and DLB showed the largest positive and negative contributions, respectively (error bars defined by 95% CI). **c**) Surface plots (lateral views of the left hemisphere) displaying the atrophy map for PS1-related dementia and the LR interaction map for FAM3C-GLRA2. Color bars indicate the strength of cell-cell communication and tissue loss, with negative values indicating tissue enlargement relative to healthy controls. **d**) Network visualization of cell-cell interactions counts from the top 10% annotated LR pairs, highlighting bi-directional signaling between neurons and endothelial cells, neurons and astrocytes, neurons and oligodendrocytes, and neurons with each other. Numbers on edges indicate counts of unique interactions. **e**) Gene enrichment analysis using the PANTHER database, indicating significant enrichment of pathways related to Slit/Robo-mediated axon guidance, enkephalin release, integrin signalling, and Alzheimer's disease presenilin ($p < 0.001$ FDR corrected).

Third axis of cell-cell interactions explains tissue atrophy patterns in PD and AD

The third axis explained 3.92% of the covariance (Fig. 5a), with prominent contributions from NPTX1-NPTXR and MET-related receptor interactions, emphasizing their association with neurodegenerative atrophy patterns. Recent findings indicate that MET protein, also known as hepatocyte growth factor receptor, is reduced in the brains of AD mice [68]. Interactions related to brain-derived neurotrophic factor (BDNF) were also prominent, as BDNF sustains synaptic plasticity and cognitive functions in healthy brains, but has been linked with Aβ accumulation, tau phosphorylation, neuroinflammation and neuronal apoptosis in AD [69,70].

Among the top six conditions contributing to the third axis (Fig. 5b), PD and bvFTD showed the largest positive weights, while LOAD and EOAD showed negative associations. These results suggest that decreased NPTX1-NPTXR and MET-related interactions may explain the atrophy patterns common to PD, bvFTD, and PNFA, while negatively associating with the atrophy observed in LOAD and EOAD.

Figure 5c illustrates brain surface maps for atrophy in PD and the spatial interaction map for NPTX1-NPTXR. Neuronal pentraxin 1 has previously been reported to be dysregulated in the brains of patients with PD [71]. NPTX2 was also present among the top 20 contributing interactions to the third axis. Neuronal pentraxin II is known to be a cerebrospinal fluid biomarker of synaptic, motor, and cognitive dysfunctions in PD [72,73]. Notably, GNAI2-DRD2 and GNAI2-DRD3 interactions, which showed strong communication across dopamine-enriched regions in Figure 2, including the substantia nigra involved in PD, were also present in the top 10% of the third axis.

Neuron-neuron interactions predominantly contributed to the third axis' patterns (37), followed by 16 neuron-astrocyte bidirectional interactions (Fig. 5d). Neuron-endothelial and endothelial-astrocyte interactions also showed significant presence (12 and 11, respectively). The

contribution from endothelial-astrocyte interactions distinguished the third axis from other axes. Gene enrichment analysis with the PANTHER database (Fig. 5e) highlighted pathways enriched in third axis. With an FDR-corrected p-value of 0.001, pathways such as enkephalin release, integrin signalling, opioid proenkephalin, and opioid prodynorphin were enriched.

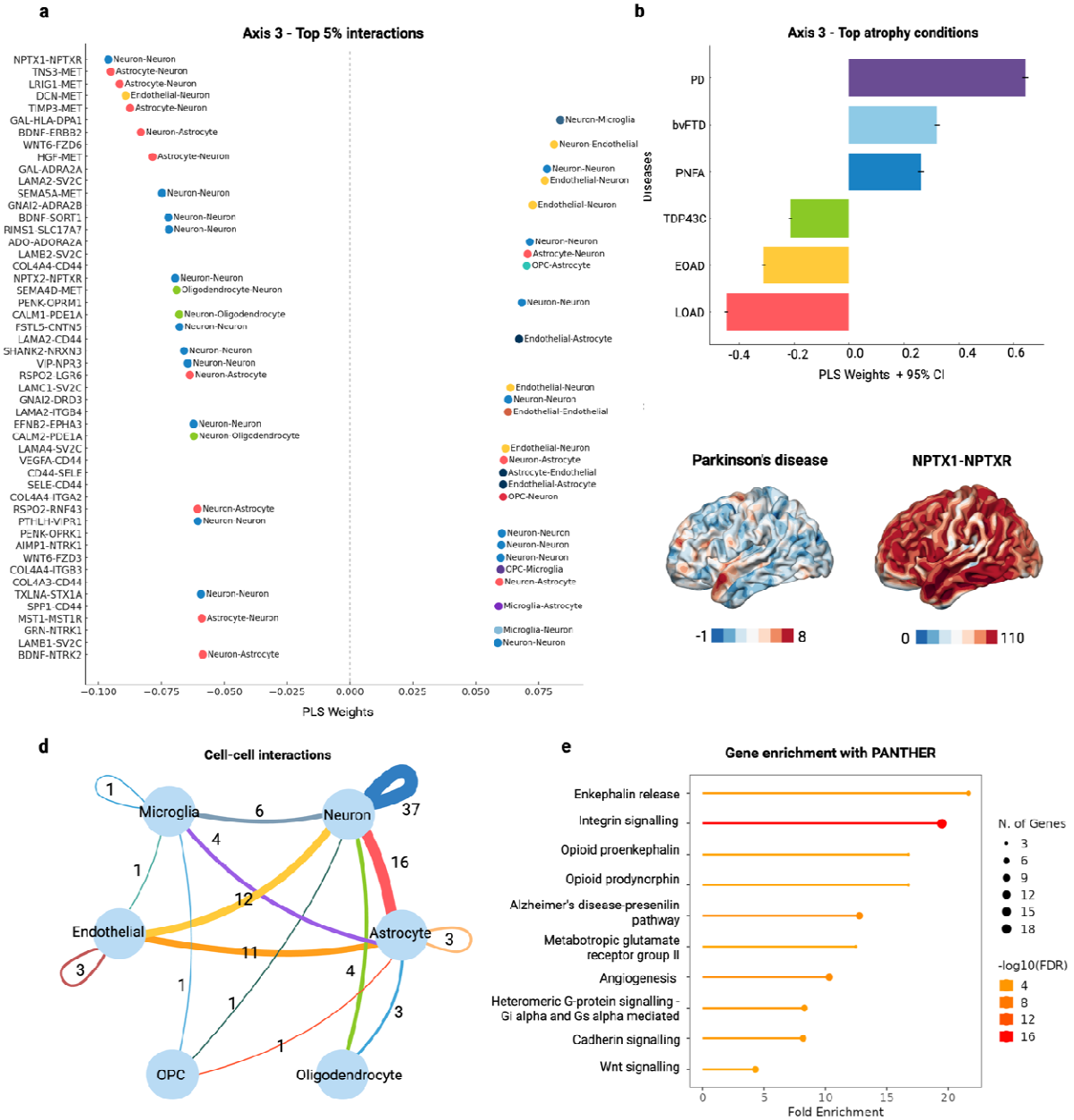

Figure 5 | Top ligand-receptor interactions and neurodegenerative conditions contributing to the third axis. **a**) PLS weights for the top 5% contributing interactions, colored by annotated cell-cell communication type, with NPTX1-NPTXR showing the highest contributions with negative weights. **b**) Top six neurodegenerative conditions with atrophy patterns explaining the third axis the most. PD showed the largest contributions with positive weights, followed by LOAD and EOAD with negative weights

(error bars defined by 95% CI). **c**) Surface plots (lateral views of the left hemisphere) displaying the atrophy map for PD and the LR interaction NPTX1-NPTXR. Color bars indicate the strength of cell-cell communication and tissue loss, with negative values indicating tissue enlargement relative to healthy controls. **d**) Network visualization of cell-cell interactions counts from the top 10% annotated LR pairs, pointing to strong bi-directional signaling between neuron-neurons and neuron-astrocytes, supporting by neuron-endothelial and endothelial-astrocyte. Numbers on edges indicate counts of unique interactions. **e**) Gene enrichment with the PANTHER database, indicated significant enrichment of pathways related to enkephalin release, integrin signalling, opioid proenkephalin, and opioid prodynorphin ($p < 0.001$ FDR corrected).

Identified cell-cell interactions in LOAD are reproduced in an independent population

Next, to validate our key findings beyond the used *in-silico* approach, we investigated whether the cell-cell interactions identified in neurotypical brains remain relevant in the context of active neurodegeneration. Our initial analyses utilized AHBA data from non-diseased neurotypical brains in conjunction with atrophy measurements from individuals with neurodegenerative conditions. This approach raises an important question: to what extent are the identified neurotypical cell-cell interaction patterns, and their associations with regional vulnerability, preserved during disease progression? To address this question, we conducted complementary validation analyses using matched transcriptomic and atrophy data from the dorsolateral prefrontal cortex (DLPFC) of 375 individuals with LOAD from the Harvard Brain Tissue Research Center (HBTRC) [74].

Atrophy measurements for the prefrontal cortex were available for all participants [74], which enabled us to apply PLS correlation using the 1003 evaluated co-expression/interaction available pairs as observations, with variations in atrophy levels as the response variable. We then run PLS correlation using 1003 equivalent interactions derived from whole-brain transcriptomic AHBA data from healthy individuals and the whole-brain atrophy map from LOAD patients. This approach was an equivalent for the main results that we applied to get the three main axes, but for LOAD only.

We analyzed the top 10% (100 pairs) from each dataset and identified 14 overlapping molecular interactions (for all PLS results, see **Supplementary Table 3**). Figure 6a lists the top 10 interactions explaining atrophy in LOAD, where LGI2-ADAM11 can be seen prominent in both datasets. Figure 6b illustrates the distribution of weights for 14 overlapping interactions across both datasets. Variations in positive and negative values across axes result from certain gene expression data in the HBTRC dataset being corrected for covariates such as sex, age, and post-mortem interval, while in AHBA-LOAD atrophy values were indicated as either positive (greater atrophy) or negative (tissue enlargement compared to controls). Nonetheless, most interactions with the same interaction labels as Astrocyte-Astrocyte, Astrocyte-Neuron and Neuron-Neuron clustered together across both datasets.

Figure 6c details the cell-cell interaction types most frequently occurring in the top 10% from both datasets. Both HBTRC and AHBA analyses demonstrated similar patterns, with neuron-neuron interactions being most frequent, followed by neuron-astrocyte and neuron-endothelial interactions. These results are different from the first axis of tissue vulnerability in several conditions (Fig. 3), where most of the interactions were captured between astrocytes and neurons, with only a few interactions between neurons and endothelial. Additionally, the AHBA-LOAD approach captured more neuron-microglia interactions (9) compared to the HBTRC (4).

Interactions between LGI2 (leucine-rich glioma inactivated 2) and the ADAM (a-disintegrin-and-metalloproteinase) family of neuronal proteins were the most prominent, explaining the association with atrophy in patients with LOAD and vulnerability to developing atrophy in LOAD. Interestingly, LGI2-ADAM22 and LGI2-ADAM11 were also in the top 10 contributing interactions to the first axis (Fig. 3). These interactions have been previously linked to epilepsy, synaptic transmission, and myelination [75-77].

Other prominent overlapping interactions mentioned earlier were APOE-GPC4 from the first axis, which drives tau hypophosphorylation [47], and NPTX1-NPTXR, which was the number one top interaction explaining atrophy in the third vulnerability axis. NPTX1 is known to play a critical role in synapse loss, neurite damage, and neuronal death induced by Aβ in LOAD [78]. Additional pairs such as BDNF-ERB2 (also contributes to the third axis) and CALM2/3-ABCA1 have also been previously linked to neurodegeneration, with reduced BDNF levels contributing to the selectivity in neuronal degeneration in AD [69] and ABCA1 regulating APOE lipidation, which affects Aβ aggregation and clearance in AD [79]. Overall, these results support that the cell-cell interactions associated with tissue vulnerability according to our *in-silico* approach, are also relevant in a large LOAD population.

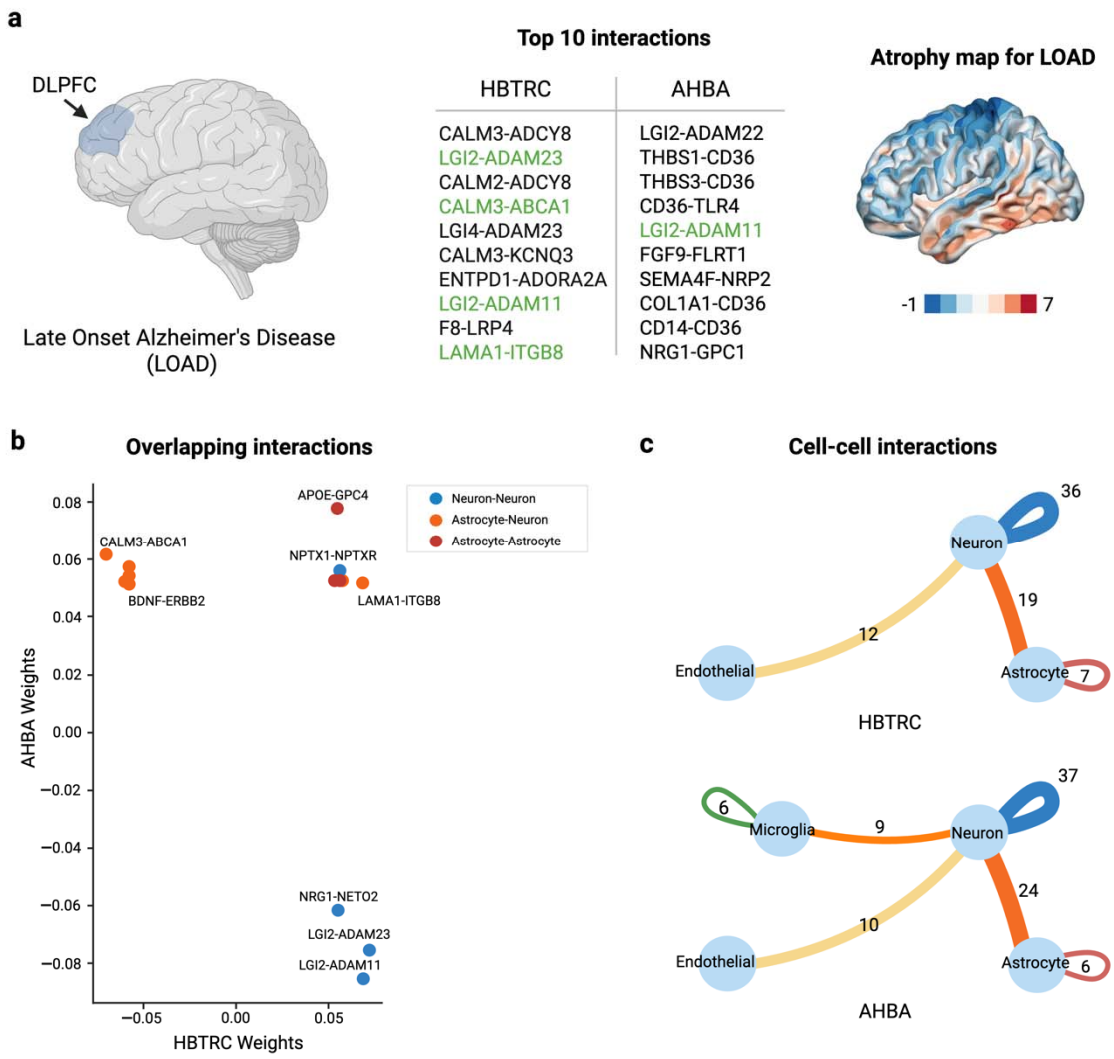

Figure 6 | Cross-validation of interactions linked to atrophy in LOAD. **a)** Top 10 interactions contributing to atrophy in the DLPFC of patients with LOAD (left) from the HBTRC dataset and in whole healthy brains (right) from the AHBA, spatially aligned with atrophy maps of LOAD. Overlapping interactions between two datasets are highlighted in green. **b)** Fourteen overlapping interactions found in the top 10% of interactions across both datasets, along with their corresponding PLS correlation weights. Pairs with the same interaction label grouped together. **c)** Cell-cell interactions (with counts >5) present in the top 10% of pairs in both the HBTRC and AHBA datasets.

Comparison with interactions derived from single-nucleus data

We assessed how spatial variation of interactions derived from bulk AHBA data across brain regions correlate with interactions derived from single-nucleus RNA-seq (snRNA-seq) data from the Allen Brain Cell (ABC) atlas [80]. The ABC atlas consists of snRNA-seq measurements from

109 regions of neurotypical human donors [80]. Interaction strengths were measured across 76 regions defined by the Allen Human Reference Atlas [81], matching those available in the ABC dataset. For ABC, gene expression was calculated specifically from the cell types corresponding to the labelled ligands and receptors that we annotated for 1,037 pairs (see Supplementary Table 1). For instance, if a gene was annotated as belonging to a specific cell type, only the expression of this gene from that particular cell type in the ABC atlas was used to calculate the cell-cell communication score. We conducted partial Spearman correlations with 500 permutations and FDR correction. Out of 1,027 ligand-receptor pairs with available genes in ABC, 409 interactions (39.82%) showed significant correlation across both datasets (a breakdown by cell type is provided in the **Supplementary Table 4**).

Of the top 10% (104 interactions) contributing to the first axis, 43 interactions showed significant alignment (positive correlation) with their snRNA-seq counterpart across regions. Figure 7a illustrates regional differences in communication scores between bulk and single-nucleus datasets. Difference values were normalized per region, with positive values indicating higher communication in AHBA interactions and negative values indicating higher expression in ABC interactions. Regions such as pons and septal nuclei (SEP) demonstrated larger differences between the two datasets compared to other regions. APOE-GPC5, SLIT-ROBO1/2, and NCAN-CDH2 demonstrated visibly higher communication in ABC interactions across many regions. Figure 7b depicts Spearman correlation coefficients (R) before permutation and FDR correction for these 43 interactions. Such pairs as SLIT-ROBO2 (R = 0.65) and PAPLN-SIRPA (R = 0.60) showed the strongest correspondence with the ABC validation set.

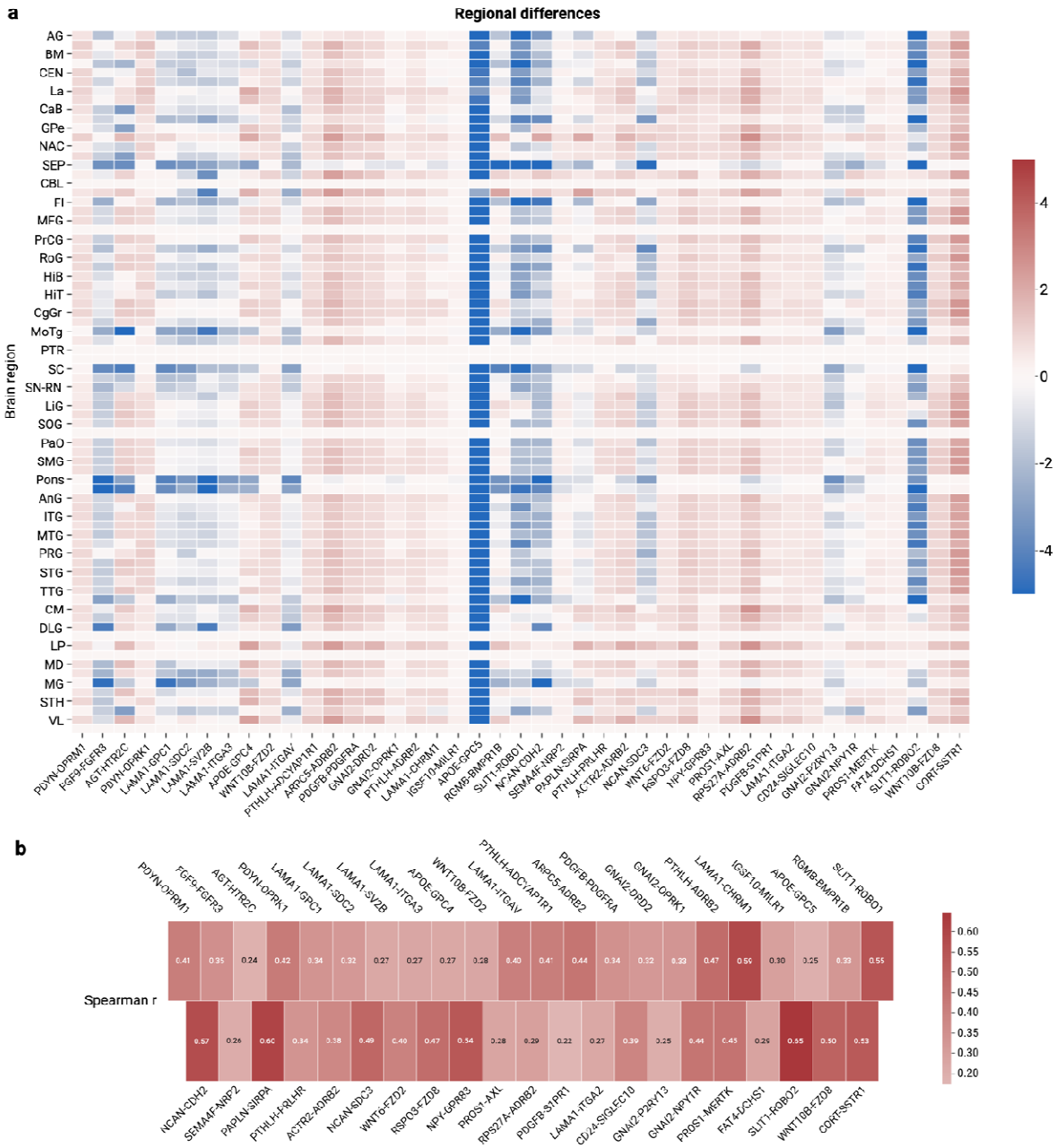

Figure 7 | Validation of bulk-derived cell-cell interactions with single-nucleus RNA-seq data from the ABC atlas. a) Heatmap illustrating regional differences in communication between bulk-derived interactions (AHBA dataset) and interactions derived from snRNA-seq data (ABC atlas). Displayed interactions (n = 43) represent the subset among the top 10% of interactions contributing to the first axis that also showed significant positive partial correlation with the single nucleus counterpart. Values were normalized for each brain region, with positive values (red) indicating higher expression in bulk data and negative values (blue) indicating higher expression in ABC data. After normalization, zero values were replaced with epsilon (light pink colour). Regions (n = 76) were defined by the Allen Human Reference atlas. **b**) Heatmap showing Spearman correlation coefficients (R) for these 43 significant interactions.

Darker shades of red indicate stronger positive correlations, demonstrating consistent spatial variation between bulk and single-nucleus data across brain regions.

Disorder commonalities across the axes of cell-cell interactions

Lastly, we investigated commonalities across the 13 conditions in terms of their contributions to the major cell-cell interaction axes. Figure 8 presents a scatter plot of the normalized PLS loadings for the 13 disorders in the 3D space, using axes 1, 2, and 3 as coordinates. Based on the Silhouette criterion applied to the K-Means algorithm, four optimal clusters of disorders were identified.

In the first cluster (dark blue), FTLD-related conditions, including 3-repeat and 4-repeat tauopathies, TDP43A pathology, and svPPA, were grouped together. Interestingly, TDP43C pathology and LOAD clustered together with DLB in the second cluster (light blue). Atrophy patterns in TDP43C explained cell-cell interactions associated with the three axes. Other FTLD conditions, such as the clinical subtypes bvFTD and PNFA, formed a separate cluster along with PD (red). Notably, both PD and DLB, which were positioned further away from the other conditions, are known synucleinopathies, unlike other conditions in this analysis that are often characterized by mixed pathologies (TDP-43, Aβ and tau).

Mutations in the PS1 clustered with EOAD and ALS, as these conditions exhibited the highest positive weights in the second axis. This finding is particularly interesting given the close relationship between EOAD and PS1 mutations, as PS1 mutations are the most common cause of autosomal dominant EOAD [82].

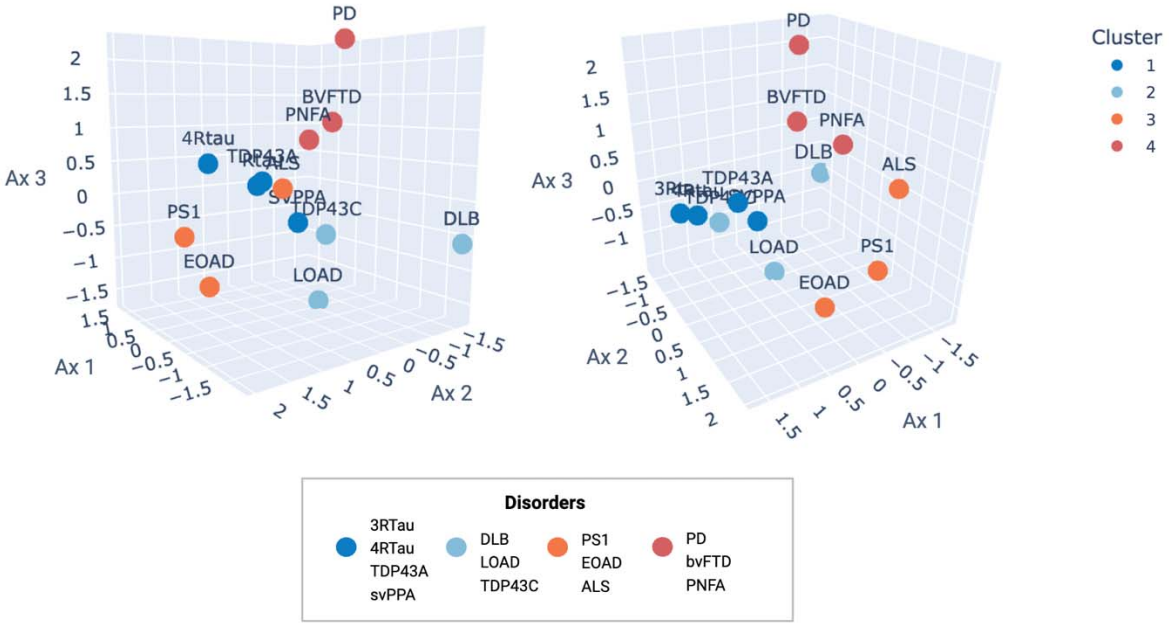

Figure 8 | Three-dimensional representation of PLS loadings across the neurodegeneration spectrum. Scatter plot illustrating the Z-score normalized PLS loadings for 13 neurodegenerative disorders in a 3D space, using axes 1, 2, and 3 as coordinates. The same plot is shown from two viewing angles to better visualize the spatial distribution of disorders. Based on Silhouette scores, K-Means clustering identified four optimal clusters: FTLD-related conditions (dark blue); TDP43C pathology, LOAD, and DLB (light blue); EOAD and ALS linked with PS1 mutations (orange); and bvFTD, PNFA, and PD (red).

DISCUSSION

The systematic characterization of cell-cell communication across the brain and multiple neurological conditions remains technically challenging. To tackle this gap, here we reconstructed whole-brain maps of more than 1,000 molecular interactions specific to major brain cell types and conducted multimodal analysis to determine how cell-cell interactions account for spatial variation in tissue atrophy across neurodegenerative conditions. This *in-silico* multimodal approach uncovered axes of whole-brain cell-cell communication significantly explaining tissue vulnerability to neurodegeneration. Notably, our complementary validation analysis in an independent LOAD cohort corroborated our initial findings. This convergence between our *in-silico* predictions and empirical observations in diseased tissues supports that the identified cellular communication networks represent crucial biological mechanisms underlying differential vulnerability across the neurodegenerative spectrum, rather than computational artifacts or coincidental associations. Together, these findings reveal the distinctive and shared cellular vulnerability across multiple neurodegenerative disorders, highlighting potential targets for therapeutic interventions.

Our results provide several key insights: (i) the first principal axis, explaining significant covariance with atrophy in subtypes of FTLD and AD, was dominated by astrocyte-neuron and astrocyte- and microglia-related interactions, such as FGF9-FGFR3 and CD36. Moreover, the first axis was enriched with various AD risk genes and genes related to regulation or spreading of Aβ and tau; ii) the second and third axes emphasized vascular endothelial-related interactions, effectively explaining atrophy patterns in mutations of PS1, EOAD, and PD, and featuring interactions like FAM3C-GLRA2, NPTX1-NPTXR, and MET; (iii) the enrichment analysis indicated that all identified axes significantly involved neurodegeneration-related biological pathways, including Slit/Robo-mediated axon guidance, enkephalin release, angiogenesis, integrin and cadherin signaling, and the Alzheimer's disease presenilin pathway; and (iv) several critical interactions, such as LGI2-ADAM23/11, identified through our method to be relevant for LOAD tissue damage, were also found associating with atrophy in the DLPFC of patients with LOAD.

Despite the observed class imbalance, with neuron-neuron interactions being predominant in our analysis, bi-directional astrocyte-neuron crosstalk played a significant role in all of our findings, consistent with recent studies on cell-cell communication in AD [83-86]. For instance, a globally downregulated astrocyte-to-excitatory-neuron signaling axis was previously identified in the postmortem prefrontal cortex (PFC) of AD patients across two independent snRNA-seq datasets [85]. Specifically, this study highlighted the downregulation of ligand-receptor pairs involving AGT, APOE, PTN, and CALM ligands. Among the top 10% of pairs from the first axis, at least 14 interactions involved AGT, APOE, and several CALM-related interactions. Increased signalling from astrocytes to excitatory glutamatergic neurons was also observed in the entorhinal cortex of both patients with AD and 5xFAD mice [86]. Another snRNA study encompassing six brain regions in AD patients identified astrocytes, alongside both inhibitory and excitatory neurons, as exhibiting the most extensive gene expression changes across all regions[87]. These findings collectively align with our prior research showing that the cell abundance of astrocytes and microglia are strong predictors of regional atrophy across multiple neurodegenerative conditions [88].

The identified molecules, along with their associated cell types and signaling pathways, represent promising therapeutic targets for individual or multiple neurodegenerative conditions. The first axis included communication among several well-established AD risk genes, such as APOE, APP, APOC1, ABCA1, CD36, and TLR4. Importantly, previous studies investigating neuron-glial interactions in the PFC of AD patients across three independent snRNA-seq datasets have also identified APOE and APP among the most common interactions [89]. However, the role of several other identified interactions in our study has been limited or less established in the context of neurodegeneration and may need further investigation by the scientific community. For instance, molecules such as FGF9 and BDNF have previously been associated with atrophy and neuronal loss in neurodegeneration [49,69]. Molecules from the top interactions with the biggest contributions to the axes, such as COL1A1-CD36, FAM3C-GLRA2 and NPTX1-NPTXR, have

been studied in neurodegeneration individually [39,65,72], but their specific roles as interactive pairs influencing atrophy have not yet been explored. Finally, the interactions between LGI and ADAM families have been prominent in both axes of vulnerability and in independent dataset for LOAD from the HBTRC, yet their specific involvement in neurodegeneration has yet to be studied.

This study presents a number of limitations. We analyzed stereotypical atrophy patterns from diverse studies with varying protocols and methodologies. The interpolated gene expression values used for cell-cell interaction measures represent approximations that may smooth over important local cellular distinctions. The genes that we studied may be expressed across multiple cell types, suggesting cautious interpretation of cell-cell interaction annotations. To mitigate this concern, we included only genes consistently annotated across multiple databases. Our use of bulk RNA sequencing data limited resolution of cell-to-cell variability, and validation with snRNA-seq confirmed only 40% of interactions, suggesting that more comprehensive future validation with single-cell/single-nucleus sequencing may enhance cell-cell communication measure and cell-type annotation accuracy. The literature-curated databases we employed showed significant class imbalance, with neuron-neuron interactions overrepresented compared to those involving non-neuronal cells, potentially leaving important non-neuronal communication patterns, such as oligodendrocyte-related interactions, undetected. Moreover, the number of cell-cell interactions used in our analysis may not accurately reflect their true biological abundance; for instance, while we have more neuron-endothelial interactions, astrocyte-neuron interactions are likely more prevalent in vivo. Finally, most literature-based interpretations focused primarily on AD, underscoring the need for expanded investigation of identified interactions in other neurodegenerative conditions, particularly frontotemporal lobar degeneration.

In addition, we used AHBA as our main dataset because it provides whole brain coverage for gene expression data, enabling us to create spatially continuous maps of cell-cell interactions that can be aligned with neuroimaging phenotypes of neurodegeneration. This spatial coverage was essential for linking cell-cell communication more accurately to atrophy patterns across neurodegenerative conditions and for creating maps that can be used by the neuroimaging community. In contrast, the ABC atlas offers higher-resolution single-nucleus data but is limited in spatial coverage of only 109 regions, so we used it for validation to confirm that key region-specific interaction patterns from AHBA were consistent at the cellular level. Several factors likely contributed to only 39.82% of interactions significantly correlating between bulk AHBA and single-nucleus ABC datasets. Firstly, methodological differences exist between the datasets: AHBA data were acquired at voxel-wise resolution, capturing expressions from multiple cell types, and subsequently averaged to represent regional expression, whereas ABC data were obtained at the individual cell level with higher resolution. Other fundamental differences between bulk and single-cell methods, including differences in preprocessing, normalization techniques, and sequencing depth, likely introduced additional variance. Second, snRNA-seq

data from ABC inherently contains dropout events, resulting in zero-expression values due to technical limitations, which could distort the values during averaging regional expression. Third, differences in the exact brain regions sampled, variations in anatomical definitions between atlases, and discrepancies in region size may have contributed. Some regions defined in the Allen Human Brain Atlas included larger anatomical areas than those covered in the ABC dataset, requiring us to average gene expression across some ABC regions to obtain a comparable counterpart, potentially diluting region-specific signals. Fourth, demographic or biological variations between participant groups (e.g., age, sex, genetic background, and cause of death) could further reduce correlation. The authors of the ABC study noted the difficulty with replicating samples across donors [80]. Thus, genes with highly dynamic or context-dependent expression, such as those involved in activity-dependent signaling, stress responses, or circadian regulation, may exhibit greater variability across individuals, reducing the consistency of regional patterns between datasets.

Our study also has several strengths. First, our method explores global spatial patterns of whole-brain cell-cell interactions linked to various conditions in a systematic way, providing a viable alternative until direct whole-brain sequencing of both healthy and diseased brains becomes feasible. Second, it correctly replicates known interactions in AD, FTD, and PD, as validated by existing literature, suggesting its capability in capturing biologically meaningful interactions. Third, our validation analysis demonstrated the biological accuracy of our reconstructed dopamine-related interaction maps, highlighting enhanced communication within established dopaminergic pathways. Fourth, we validated specific LOAD-related interactions identified from healthy brains by demonstrating their alignment with atrophy patterns in the DLPFC from disease participants. Lastly, our study examined commonalities in molecular interaction patterns across distinct and related neurodegenerative conditions, where subtypes of the same condition (e.g., FTLD) or genetically related disorders (e.g., EOAD and PS1) showed similar patterns. Importantly, the generated maps of ligand-receptor interactions are freely shared with the research community. Combined with the multimodal PLS tools (also available at our lab's GitHub), these maps can serve as a scalable tool for investigating molecular basis of brain phenotypes and also less-studied neurological conditions, such as psychiatric disorders, generating new hypotheses, and guiding experimental follow-up.

METHODS

Allen Human Brain Atlas

Bulk microarray messenger RNA (mRNA) expression data from the Allen Human Brain Atlas (AHBA; https://human.brain-map.org/) was used to construct interaction mapsc [23]. This included anatomical and histological data collected post-mortem from six healthy individuals with no history of neurological disease (one female; age range 24–57 years; mean age 42.5 ± 13.38 years) [23]. Data from two donors covered the entire brain, while the remaining four included the

left hemisphere only. A total of 3,702 spatially distinct samples were distributed across cortical, subcortical, brainstem, and cerebellar regions, with expression levels measured for over 20,000 genes [23]. Each brain sample is labeled with native MRI coordinates [90] and Montreal Neurological Institute (MNI) coordinates [30], based on structural magnetic resonance (MR) images collected from the same participants, allowing precise alignment of samples with imaging data. Data were initially preprocessed by the Allen Institute to reduce the effects of bias due to batch effects [23].

To estimate gene expression levels at unsampled brain locations, we applied Gaussian process regression, a previously validated method to interpolate AHBA data across the whole brain [22]. This approach allows the prediction of mRNA expression levels for all gray matter (GM) voxels in the standardized MNI brain space [30]. Gaussian process regression predicts gene expression in unobserved regions using values from neighboring sampled regions, with weights decreasing as distance increases.

Harvard Brain Tissue Resource Center

Adjusted gene expression data from autopsied DLPFC brain tissue of LOAD patients were obtained from the Gene Expression Omnibus (GEO) database under accession number GSE44770. This dataset included detailed demographic information, disease states, and measurements of brain atrophy [74]. Brain tissue samples were originally collected through the Harvard Brain Tissue Resource Center (HBTRC), where all subjects underwent a comprehensive diagnostic assessment upon intake, and each brain was rigorously examined for LOAD-related neuropathology [74]. Gene expression levels had been previously adjusted to account for covariates, including age, sex, postmortem interval (PMI) in hours, sample pH, and RNA integrity number (RIN) [74]. Of the initial 379 participants with AD diagnosis, 375 were included in our analysis (mean age 80.81 ± 9.05 years; 156 males, 219 females), as complete data for both gene expression and corresponding regional atrophy in the PFC were available for these individuals.

Allen Brain Cell Atlas

The Allen Brain Cell (ABC) Atlas is a platform that explores single-cell data across the mammalian brain. In this study, we used a dataset profiling over 3 million cells from the entire adult human brain, generated using single-nucleus RNA sequencing (10x Genomics). Post-mortem brain tissue was collected from three neurotypical male donors (ages 29–60; mean age 40.33 ± 10.60 years) with no known history of neuropsychiatric or neurological conditions. One additional motor cortex dissection was included from a 60-year-old female donor. The dataset includes 109 standardized dissections spanning the cerebral cortex and subcortical regions. Cells were hierarchically clustered into 31 superclusters, 461 clusters, and 3,313 subclusters. Here, we leveraged the ABC atlas to independently validate region-specific cell-cell interactions identified using bulk transcriptomic data from AHBA.

Ligand-receptor interaction databases

Databases of interaction pairs were obtained from the "Compendium of Available Lists of Ligand-Receptor Pairs in Literature" curated by Armingol et al. in their systematic review of cell-cell communication inference methods [24]. Ten databases of LR pairs specific to human tissues were selected [25,91-98], including NeuronChatDB, which focuses on neuronal interactions [99]. Ligand-receptor pairs involving composite multi-gene complexes or cofactors were excluded or split into individual gene-level pairs to maintain consistent one-to-one gene pair formatting. After concatenating all pairs across databases, we compiled a unique list of genes corresponding to ligands and receptors. This list was cross-referenced with the AHBA database of approximately 20,000 genes, resulting in 5,551 ligand-receptor pairs available.

Cell type annotation

To capture interactions only relevant to the human brain, we limited our analysis to genes corresponding to ligands and receptors frequently expressed in six major brain cell types: neurons, astrocytes, microglia, endothelial cells, oligodendrocytes, and oligodendrocyte precursor cells. Previous efforts to select cell-type-specific genes from AHBA have included the integration of five different single-cell studies using postmortem cortical samples from human postnatal subjects [100]. To create a more time- and computationally efficient approach, we developed the R package BrainCellAnn, which integrates comprehensive reference databases of gene markers specific to cell types in the human brain.

The package estimates consensus cell types through comparing outputs from different databases, ensuring specificity and reliability. The first database used was the R package BRETIGEA, which includes brain gene markers from five RNA-seq studies, validated by ATAC-seq and immunohistochemistry analyses on the same brain samples [28]. The second resource was the PanglaoDB database of curated gene signatures, integrated into the OmniPath [101] and decoupleR [102] R packages. PanglaoDB contains pre-processed meta-analyses from over 1,054 scRNA-seq experiments, covering a wide range of tissues and organs [27]. Thirdly, we used the CellMarker 2.0 database [26], which provides a manually curated collection of experimentally supported markers for various cell types in human and mouse tissues, including markers from approximately 102,000 studies in PubMed and cells derived from 48 single-cell RNA-seq studies. The final resources were the immunohistochemistry and single-cell datasets from the Human Protein Atlas (HPA), the largest and most comprehensive web database providing information on protein expression and localization across human tissues and cells [29].

The algorithm takes a list of gene markers as input, then each database returns one or two most likely candidate cell types. For a cell type to reach consensus, it should be labelled in agreement with at least two databases. The consensus score is calculated based on number of appearances of a cell type per database and database-specific weights. In cases of consensus conflict, database-specific weights are ranked using Random Forest feature importance to match cell type

annotations from the Allen Institute's ABC Whole-Brain Human Atlas [80], prioritizing certain databases for specific cell types over others.

Out of 5,551 interaction pairs, only 1,037 had both the ligand and receptor consistently annotated by at least two databases. Considerations for immune cells were made, so cell type annotation algorithm would not include gene known to be highly expressed in T cells, B cells, and Natural Killer cells.

Reconstruction of interaction maps

Most methods for inferring cell-cell communication from gene expression data have been developed for single-cell data [24]. Methods such as CellPhoneDB [103], Connectome [104], NATMI [91], and ICELLNET [96] incorporate the product of ligand and receptor expression levels as a measure of communication. Similarly, in the AHBA bulk data we use here, cell-cell communication was calculated by multiplying the expression level of a ligand in an individual voxel (1.5 x 1.5 x 1.5 mm^3 size) by the expression level of the corresponding receptor in the same voxel:

$$Voxel_i = L_i \times R_i,$$

where *i* represents an individual voxel (i = 1, 2, ..., n), *L* is the expression level of a ligand in the voxel, and *R* is the expression level of a receptor gene in the voxel. The communication strength reflects co-expression of ligands and receptors within mixed cell populations.

Interactions between individual ligand-receptor pairs were estimated across all gray matter voxels. For each map, interaction measures were registered into MNI and volumetric space using the ICBM152 template [30].

For the ABC dataset, gene expression was measured specifically from the cell type corresponding to each annotated ligand or receptor in the 1,037 interaction pairs. For each gene, expression from the relevant cell type was first averaged across regions, and then, for each interacting pair, the ligand and receptor regional expression values were multiplied.

Disorder-specific atrophy maps

We obtained whole-brain voxel-wise atrophy maps for thirteen neurodegenerative conditions, including early- and late-onset Alzheimer's disease (EOAD and LOAD, respectively), Parkinson's disease (PD), amyotrophic lateral sclerosis (ALS), dementia with Lewy bodies (DLB), mutations in presenilin-1 (PS-1), clinical variants of frontotemporal dementia (the behavioural variant bvFTD and the non-fluent and semantic variants of primary progressive aphasia nfvPPA and svPPA), and FTLD-related pathologies such as FLTD-TDP (TAR DNA-binding protein) types A and C, 3-repeat tauopathy, and 4-repeat tauopathy [18-20]. The term FTD was used when addressing the clinical syndromes, and the term FTLD when referencing the histologically confirmed neurodegenerative pathologies [105]. Changes in tissue density in the

atrophy maps were measured by voxel- and deformation-based morphometry (VBM and DBM) applied to structural T1-weighted MR images, and expressed as a t-score per voxel (relatively low negative values indicate greater GM tissue loss/atrophy) [106,107]. VBM is a data-driven technique to identify regional differences in tissue concentration throughout the whole brain, without requiring predefined regions of interest [106]. DBM is related method for detecting structural brain changes across participants, which in addition considers anatomical differences such as shape and size of brain structures [107]. **Supplementary Table 5** summarizes origin of each disorder-related atrophy map compiled from different studies. Initially, all atrophy maps except for PD had negative values indicating atrophy and positive values indicating tissue enlargement compared to controls; however, these values were reversed for an easier and more intuitive interpretation of their relationships with LR interactions in the Results section.

MRI data for neuropathological dementias were obtained from 186 individuals with clinically diagnosed dementia, confirmed by histopathological examination (either postmortem or biopsy), along with 73 cognitively healthy controls [18]. Data were averaged by condition: 107 participants had a primary diagnosis of Alzheimer's disease (AD) (including 68 with early-onset [<65 years at onset], 29 with late-onset [≥65 years at onset], and 10 carriers of the PS1 mutation), 25 had dementia with Lewy bodies (DLB), 11 had three-repeat tauopathy, 17 had four-repeat tauopathy, 12 had frontotemporal lobar degeneration with TDP-43 type A (FTLD-TDP type A), and 14 had FTLD-TDP type C [18]. T1-weighted volumetric MRI data were collected from participants during life across multiple centers, using scanners from three manufacturers (Philips, GE, and Siemens) with different imaging protocols [18]. Magnetic field strengths included 1.0 T (15 scans), 1.5 T (201 scans), and 3 T (43 scans) [18]. Pathological examination of brain tissue took place between 1997 and 2015, following standard histopathological procedures and criteria at one of four centers: the Queen Square Brain Bank in London, Kings College Hospital in London, VU Medical Centre in Amsterdam, and the Institute for Ageing and Health in Newcastle [18]. Atrophy maps were statistically adjusted for age, sex, total intracranial volume, and MRI field strength and site [18]. Ethical approval for the corresponding study was provided by the National Research Ethics Service Committee London-Southeast [18].

For PD, MRI data were obtained from the Parkinson’s Progression Markers Initiative (PPMI) database [19,108]. The PPMI is a multicenter international study with acquisition protocols approved by the local institutional review boards at all 24 sites across the United States, Europe, and Australia [108]. Imaging data were collected at 16 centers participating in the PPMI project, using scanners from three different manufacturers (GE Medical Systems, Siemens, and Philips Medical Systems) [108]. High-resolution 3T T1-weighted MRI scans from the initial visit, along with clinical data used to construct atrophy maps, were acquired from 232 participants with PD and 118 age-matched controls [19]. PD subjects (77 females; age 61.2 ± 9.1) were required to be at least 30 years old, untreated with PD medications, diagnosed within the last two years, and exhibit at least two PD-related motor symptoms, such as asymmetrical resting tremor, uneven bradykinesia, or a combination of bradykinesia, resting tremor, and rigidity [108]. All participants

underwent dopamine transporter (DAT) imaging to confirm a DAT deficit as a prerequisite for eligibility [108]. Written informed consent was collected from all study participants [108].

MRI data from ALS patients were obtained from 66 individuals (24 females; age 57.98 ± 10.84), as well as 43 matched control individuals, who participated in the longitudinal study through the Canadian ALS Neuroimaging Consortium (ClinicalTrials.gov NCT02405182) [20,109]. This consortium includes 3T MRI sites at the University of Alberta, University of Calgary, University of Toronto, and McGill University [109]. Patients were eligible if they were diagnosed with sporadic or familial ALS and met the revised research criteria from El Escorial [110] for possible, laboratory-supported, or definite ALS [109]. Neurological examination was conducted by a trained neurologist at each participating site [109]. Clinical evaluations included global measures of disease status, upper motor neuron dysfunction and cognitive batteries [109]. Written informed consent was obtained from all participants, and the study received ethical approval from the health research ethics boards at each center [109]. Exclusion criteria included a history of other neurological or psychiatric disorders, prior brain injury, or respiratory impairment that prevented tolerance of the MRI protocol [109]. Patients with primary lateral sclerosis, progressive muscular atrophy, or FTD were also excluded [109]. Before constructing the maps, normative aging and sex differences were regressed out of the data [20].

For clinical subtypes of FTD, data were examined from the Frontotemporal Lobar Degeneration Neuroimaging Initiative (FTLDNI AG032306), part of the ALLFTD initiative. Atrophy maps were constructed using data from 136 FTD patients and 133 age-matched control participants [21]. Participants were grouped according to their FTD clinical variant: 70 were diagnosed with the behavioral variant, 36 with semantic primary progressive aphasia, and 30 with non-fluent primary progressive aphasia [21,111]. Structural 3T MRI scans were acquired at three locations: University of California San Francisco, Mayo Clinic, and Massachusetts General Hospital [111]. Patients were either referred by physicians or self-referred and underwent comprehensive neurological, neuropsychological, and functional assessments, including informant interviews [111]. Diagnoses were established during multidisciplinary consensus conferences based on either the Neary criteria [112] or, depending on enrollment year, the more recent consensus criteria for bvFTD [113] and PPA [114]. Histological analysis was also conducted to assess potential Alzheimer's disease pathology, due to overlapping clinical symptoms between the conditions [111]. All participants provided informed consent, and the study protocol received institutional review board approval at each site [111].

Anatomical parcellations

Two anatomical parcellations were used to define regions of interest in the validation analyses. The Desikan-Killiany-Tourville (DKT) parcellation included 62 distinct cortical regions, which were averaged across both left and right hemispheres [37,38]. We manually added several subcortical structures from FreeSurfer segmentation, including the subthalamic nucleus, red

nucleus, dentate nucleus, and substantia nigra. After excluding regions with missing values in the cell-cell interaction maps, we used 44 regions for validating dopamine-related interaction maps.

The Allen Human Reference Atlas included 141 brain regions from both hemispheres of the adult human brain [81]. Many of these regions corresponded to modified Brodmann areas and were designed to reflect cellular resolution in histological images, helping to link microscopic features with the macroscopic scales more common in neuroimaging studies [81]. This atlas was also used to define many of the regions included in the ABC atlas, which we used to validate our bulk-derived cell-cell interactions [80]. In total, we used 76 brain regions that overlapped between the ABC atlas and the Allen Human Reference Atlas and were available in our cell-cell interaction maps.

Partial least squares analyses

Multidimensional associations between atrophy patterns specific to 13 neurodegenerative conditions and 1,037 LR interaction scores were evaluated using partial least squares (PLS) cross-correlation analysis [115-117]. PLS correlation, a data reduction technique related to principal component analysis (PCA), uses singular value decomposition (SVD) on the covariance matrix of two datasets (X and Y) to identify linear combinations of the original variables that optimally covary [116,117].

Mathematically, the SVD of the covariance matrix is expressed as:

$$C_{XY} = U \sum V^T$$

where U and V represent orthogonal matrices containing the singular vectors, and $\sum$ is a diagonal matrix containing the singular values indicating the strength of covariation.

We applied PLS correlation to rank interactions based on their multivariate spatial alignment with atrophy patterns across 13 neurodegenerative conditions. Unlike PCA, which maximizes variance within a single dataset (X), PLS maximizes the covariance between two datasets (X and Y), where X represents interactions, and Y represents atrophy patterns.

Specifically, PLS seeks weight vectors w_X and w_Y to maximize:

$$Cov(X_{w_x}, Y_{w_Y})$$

The resulting weights and factor scores ensure maximum covariance, facilitating the identification of molecular interactions most closely aligned with disease-specific atrophy patterns. The top 10% (104 of the 1,037 interactions) with the largest absolute weights were selected for downstream analysis and interpretation.

To assess the statistical significance of each PLS-derived LV or axis, random permutation testing and bootstrapping were performed with 1,000 iterations each. Permutation testing provided family-wise error (FWE) corrected p-values for each axis, while bootstrapping was used to estimate the contribution of each original variable. Confidence intervals (CI) were calculated to confirm the robustness of these contribution scores (weights).

Enrichment analysis with PANTHER

The PANTHER database was used to identify enriched pathways specific to cell signalling that associate with the genes corresponding to top 10% ligands and receptors [58]. Gene-set enrichment analysis was conducted using the ShinyGO web tool [118]. The enrichment results were reported as −10log(p-value), with a false discovery rate (FDR) cutoff of 0.01 applied to control for multiple testing. This cutoff ensured that only highly significant pathways were reported in the results.

Data and materials availability: Gene expression data from the Allen Human Brain Atlas are publicly available at https://human.brain-map.org/static/download. Gene expression data from autopsied prefrontal cortex tissue of patients with late-onset Alzheimer's disease, along with associated demographic and clinical information, are available from the Gene Expression Omnibus (GEO accession number: GSE44770, a subset of GSE44772). Atrophy maps for pathologically confirmed dementias can be accessed via NeuroVault (Collection ID: 1818) at https://identifiers.org/neurovault.collection:1818. Raw demographic and MRI data from Parkinson's disease and amyotrophic lateral sclerosis (ALS) patients are available through the PPMI database (https://www.ppmi-info.org) and CALSNIC (http://calsnic.org; ClinicalTrials.gov Identifier: NCT02405182), respectively. Atrophy maps for clinical variants of frontotemporal dementia (FTD) are deposited on Zenodo at https://doi.org/10.5281/zenodo.10383492. Data from the FTLDNI initiative are available through the Laboratory of Neuroimaging (LONI) Image Data Archive (https://ida.loni.usc.edu). Curated databases of ligand–receptor interactions were retrieved from https://github.com/LewisLabUCSD/Ligand-Receptor-Pairs. MATLAB code for cross-correlational partial least squares (PLS) analysis is available at https://github.com/neuropm-lab/svd_pls. Over one thousand whole-brain maps of cell–cell interactions generated in this study will be made available on Zenodo upon publication. The braincellann R package for annotating brain-specific gene markers by cell type is available at https://github.com/nikaxpak/braincellann.

Acknowledgments: This project was partly supported by the following awards to YIM: Canada Research Chair tier-2, NSERC Discovery grant, CIHR Project Grant 2020, and Weston Family Foundation's Transformational Research in AD 2020. VP was mainly supported by the Fonds de recherche du Québec (FRQ) doctoral scholarship and the Laszlo & Etelka Kollar Fellowship from the Faculty of Medicine and Health Sciences at McGill University and partly supported by

the HBHL's Theme 1 Discovery fund 2022–2025. We used the computational infrastructure of the McConnell Brain Imaging Center, supported in part by the *Brain Canada Foundation*.

References

1 Balusu, S., Praschberger, R., Lauwers, E., De Strooper, B. & Verstreken, P. Neurodegeneration cell per cell. *Neuron* **111**, 767-786 (2023). https://doi.org/10.1016/j.neuron.2023.01.016

2 Green, G. S. *et al.* Cellular communities reveal trajectories of brain ageing and Alzheimer's disease. *Nature* **633**, 634-645 (2024). https://doi.org/10.1038/s41586-024-07871-6

3 Gorman, A. M. Neuronal cell death in neurodegenerative diseases: recurring themes around protein handling. *Journal of Cellular and Molecular Medicine* **12** (2008). https://doi.org/10.1111/j.1582-4934.2008.00402.x

4 Brandebura, A. N., Paumier, A., Onur, T. S. & Allen, N. J. Astrocyte contribution to dysfunction, risk and progression in neurodegenerative disorders. *Nature Reviews Neuroscience* **24**, 23-39 (2023). https://doi.org/10.1038/s41583-022-00641-1

5 Gao, C., Jiang, J., Tan, Y. & Chen, S. Microglia in neurodegenerative diseases: mechanism and potential therapeutic targets. *Signal Transduction and Targeted Therapy* **8** (2023). https://doi.org/10.1038/s41392-023-01588-0

6 Park, H. *et al.* Single-cell RNA-sequencing identifies disease-associated oligodendrocytes in male APP NL-G-F and 5XFAD mice. *Nature Communications* **14** (2023). https://doi.org/10.1038/s41467-023-36519-8

7 Patani, R., Hardingham, G. E. & Liddelow, S. A. Functional roles of reactive astrocytes in neuroinflammation and neurodegeneration. *Nature Reviews Neurology* **19**, 395-409 (2023). https://doi.org/10.1038/s41582-023-00822-1

8 Mathys, H. *et al.* Single-cell transcriptomic analysis of Alzheimer's disease. *Nature* **570**, 332-337 (2019). https://doi.org/10.1038/s41586-019-1195-2

9 Li, J. *et al.* Divergent single cell transcriptome and epigenome alterations in ALS and FTD patients with C9orf72 mutation. *Nat Commun* **14**, 5714 (2023). https://doi.org/10.1038/s41467-023-41033-y

10 Martirosyan, A. *et al.* Unravelling cell type-specific responses to Parkinson's Disease at single cell resolution. *Mol Neurodegener* **19**, 7 (2024). https://doi.org/10.1186/s13024-023-00699-0

11 Su, J. *et al.* Cell-cell communication: new insights and clinical implications. *Signal Transduct Target Ther* **9**, 196 (2024). https://doi.org/10.1038/s41392-024-01888-z

12 Chi, X. *et al.* Astrocyte-neuron communication through the complement C3-C3aR pathway in Parkinson's disease. *Brain Behav Immun* **123**, 229-243 (2025). https://doi.org/10.1016/j.bbi.2024.09.022

13 Cihankaya, H., Theiss, C. & Matschke, V. Significance of intercellular communication for neurodegenerative diseases. *Neural Regen Res* **17**, 1015-1017 (2022). https://doi.org/10.4103/1673-5374.324840

14 Saavedra, J., Nascimento, M., Liz, M. A. & Cardoso, I. Key brain cell interactions and contributions to the pathogenesis of Alzheimer's disease. *Front Cell Dev Biol* **10**, 1036123 (2022). https://doi.org/10.3389/fcell.2022.1036123

15 Armingol, E. *et al.* The diversification of methods for studying cell–cell interactions and communication. *Nature Reviews Genetics* **25** (2024). https://doi.org/10.1038/s41576-023-00685-8

16 Armingol, E. *et al.* Deciphering cell–cell interactions and communication from gene expression. *Nature Reviews Genetics* **22** (2020). https://doi.org/10.1038/s41576-020-00292-x

17 Pandya, V. A. & Patani, R. Region-specific vulnerability in neurodegeneration: lessons from normal ageing. *Ageing Res Rev* **67**, 101311 (2021). https://doi.org/10.1016/j.arr.2021.101311

18 Harper, L. *et al.* Patterns of atrophy in pathologically confirmed dementias: a voxelwise analysis. *J Neurol Neurosurg Psychiatry* **88**, 908-916 (2017). https://doi.org/10.1136/jnnp-2016-314978

19 Zeighami, Y. *et al.* Network structure of brain atrophy in de novo Parkinson's disease. *Elife* **4** (2015). https://doi.org/10.7554/eLife.08440

20 Dadar, M. *et al.* Cerebral atrophy in amyotrophic lateral sclerosis parallels the pathological distribution of TDP43. *Brain Commun* **2**, fcaa061 (2020). https://doi.org/10.1093/braincomms/fcaa061
21 Metz, A., Zeighami, Y., Ducharme, S., Villeneuve, S. & Dadar, M. Frontotemporal dementia subtyping using machine learning, multivariate statistics and neuroimaging. *Brain Commun* **7**, fcaf065 (2025). https://doi.org/10.1093/braincomms/fcaf065
22 Gryglewski, G. *et al.* Spatial analysis and high resolution mapping of the human whole-brain transcriptome for integrative analysis in neuroimaging. *Neuroimage* **176**, 259-267 (2018). https://doi.org/10.1016/j.neuroimage.2018.04.068
23 Hawrylycz, M. J. *et al.* An anatomically comprehensive atlas of the adult human brain transcriptome. *Nature* **489**, 391-399 (2012). https://doi.org/10.1038/nature11405
24 Armingol, E., Officer, A., Harismendy, O. & Lewis, N. E. Deciphering cell-cell interactions and communication from gene expression. *Nat Rev Genet* **22**, 71-88 (2021). https://doi.org/10.1038/s41576-020-00292-x
25 Ramilowski, J. A. *et al.* A draft network of ligand-receptor-mediated multicellular signalling in human. *Nat Commun* **6**, 7866 (2015). https://doi.org/10.1038/ncomms8866
26 Hu, C. *et al.* CellMarker 2.0: an updated database of manually curated cell markers in human/mouse and web tools based on scRNA-seq data. *Nucleic Acids Res* **51**, D870-d876 (2023). https://doi.org/10.1093/nar/gkac947
27 Franzén, O., Gan, L. M. & Björkegren, J. L. M. PanglaoDB: a web server for exploration of mouse and human single-cell RNA sequencing data. *Database (Oxford)* **2019** (2019). https://doi.org/10.1093/database/baz046
28 McKenzie, A. T. *et al.* Brain Cell Type Specific Gene Expression and Co-expression Network Architectures. *Sci Rep* **8**, 8868 (2018). https://doi.org/10.1038/s41598-018-27293-5
29 Thul, P. J. & Lindskog, C. The human protein atlas: A spatial map of the human proteome. *Protein Sci* **27**, 233-244 (2018). https://doi.org/10.1002/pro.3307
30 Evans, A. C., Kamber, M., Collins, D. L. & MacDonald, D. in *Magnetic Resonance Scanning and Epilepsy* (eds S. D. Shorvon *et al.*) 263-274 (Springer US, 1994).
31 Pinson, K. I., Brennan, J., Monkley, S., Avery, B. J. & Skarnes, W. C. An LDL-receptor-related protein mediates Wnt signalling in mice. *Nature* **407**, 535-538 (2000). https://doi.org/10.1038/35035124
32 Janz, R., Goda, Y., Geppert, M., Missler, M. & Südhof, T. C. SV2A and SV2B Function as Redundant Ca2+ Regulators in Neurotransmitter Release. *Neuron* **24**, 1003-1016 (1999). https://doi.org/10.1016/s0896-6273(00)81046-6
33 Laudon, H. *et al.* A nine-transmembrane domain topology for presenilin 1. *J Biol Chem* **280**, 35352-35360 (2005). https://doi.org/10.1074/jbc.M507217200
34 Shao, X. *et al.* CellTalkDB: a manually curated database of ligand–receptor interactions in humans and mice. *Briefings in Bioinformatics* **22** (2021). https://doi.org/10.1093/bib/bbaa269
35 Magovcevic, I. *et al.* Regional localization of the human G protein αi2 (GNAI2) gene: Assignment to 3p21 and a related sequence (GNAI2L) to 12p12–p13. *Genomics* **12** (1992). https://doi.org/10.1016/0888-7543(92)90414-N
36 Surratt, C. K. *et al.* A human synaptic vesicle monoamine transporter cDNA predicts posttranslational modifications, reveals chromosome 10 gene localization and identifies TaqI RFLPs. *FEBS Letters* **318**, 325-330 (1993). https://doi.org/https://doi.org/10.1016/0014-5793(93)80539-7
37 Desikan, R. S. *et al.* An automated labeling system for subdividing the human cerebral cortex on MRI scans into gyral based regions of interest. *Neuroimage* **31**, 968-980 (2006). https://doi.org/10.1016/j.neuroimage.2006.01.021
38 Klein, A. & Tourville, J. 101 labeled brain images and a consistent human cortical labeling protocol. *Front Neurosci* **6**, 171 (2012). https://doi.org/10.3389/fnins.2012.00171

39 Dobri, A. M., Dudău, M., Enciu, A. M. & Hinescu, M. E. CD36 in Alzheimer's Disease: An Overview of Molecular Mechanisms and Therapeutic Targeting. *Neuroscience* **453**, 301-311 (2021). https://doi.org/10.1016/j.neuroscience.2020.11.003
40 Feng, M. *et al.* Role of CD36 in central nervous system diseases. *Neural Regen Res* **19**, 512-518 (2024). https://doi.org/10.4103/1673-5374.380821
41 Park, L. *et al.* Scavenger receptor CD36 is essential for the cerebrovascular oxidative stress and neurovascular dysfunction induced by amyloid-beta. *Proc Natl Acad Sci U S A* **108**, 5063-5068 (2011). https://doi.org/10.1073/pnas.1015413108
42 Shmuel-Galia, L. *et al.* Intramembrane attenuation of the TLR4-TLR6 dimer impairs receptor assembly and reduces microglia-mediated neurodegeneration. *J Biol Chem* **292**, 13415-13427 (2017). https://doi.org/10.1074/jbc.M117.784983
43 Kang, S., Byun, J., Son, S. M. & Mook-Jung, I. Thrombospondin-1 protects against Aβ-induced mitochondrial fragmentation and dysfunction in hippocampal cells. *Cell Death Discovery* **4** (2018). https://doi.org/10.1038/s41420-017-0023-4
44 Son, S. M. *et al.* Thrombospondin-1 prevents amyloid beta–mediated synaptic pathology in Alzheimer's disease. *Neurobiology of Aging* **36** (2015). https://doi.org/10.1016/j.neurobiolaging.2015.09.005
45 Wei, H. *et al.* Heat shock protein 90: biological functions, diseases, and therapeutic targets. *MedComm* **5** (2024). https://doi.org/10.1002/mco2.470
46 Zhou, Q. *et al.* Association between APOC1 polymorphism and Alzheimer's disease: a case-control study and meta-analysis. *PLoS One* **9**, e87017 (2014). https://doi.org/10.1371/journal.pone.0087017
47 Saroja, S. R., Gorbachev, K., Julia, T., Goate, A. M. & Pereira, A. C. Astrocyte-secreted glypican-4 drives APOE4-dependent tau hyperphosphorylation. *Proc Natl Acad Sci U S A* **119**, e2108870119 (2022). https://doi.org/10.1073/pnas.2108870119
48 Loch, R. A. *et al.* Cross interactions between Apolipoprotein E and amyloid proteins in neurodegenerative diseases. *Computational and Structural Biotechnology Journal* **21** (2023). https://doi.org/10.1016/j.csbj.2023.01.022
49 Thümmler, K. *et al.* Fibroblast growth factor 9 (FGF9)-mediated neurodegeneration: Implications for progressive multiple sclerosis? *Neuropathol Appl Neurobiol* **49**, e12935 (2023). https://doi.org/10.1111/nan.12935
50 Kim, D. K. *et al.* FGFR3 drives Abeta-induced tau uptake. *Exp Mol Med* **56**, 1631-1642 (2024). https://doi.org/10.1038/s12276-024-01274-3
51 Van Olst, L. *et al.* Microglial mechanisms drive amyloid-β clearance in immunized patients with Alzheimer’s disease. *Nature Medicine* (2025). https://doi.org/10.1038/s41591-025-03574-1
52 Kamino, K. *et al.* Genetic association study between senile dementia of Alzheimer's type and APOE/C1/C2 gene cluster. *Gerontology* **42 Suppl 1**, 12-19 (1996). https://doi.org/10.1159/000213820
53 Cudaback, E. *et al.* Apolipoprotein C-I is an APOE genotype-dependent suppressor of glial activation. *Journal of Neuroinflammation 2012 9:1* **9** (2012). https://doi.org/10.1186/1742-2094-9-192
54 Huang, C. *et al.* From Genes to Metabolites: HSP90B1's Role in Alzheimer's Disease and Potential for Therapeutic Intervention. *Neuromolecular Med* **27**, 6 (2025). https://doi.org/10.1007/s12017-024-08822-0
55 Gonzalez-Rodriguez, M. *et al.* Neurodegeneration and Astrogliosis in the Human CA1 Hippocampal Subfield Are Related to hsp90ab1 and bag3 in Alzheimer's Disease. *Int J Mol Sci* **23** (2021). https://doi.org/10.3390/ijms23010165
56 Shelton, L. B., Koren, J. & Blair, L. J. Imbalances in the Hsp90 Chaperone Machinery: Implications for Tauopathies. *Frontiers in Neuroscience* **11** (2017). https://doi.org/10.3389/fnins.2017.00724

57 Llibre-Guerra, J. J. *et al.* Longitudinal analysis of a dominantly inherited Alzheimer disease mutation carrier protected from dementia. *Nat Med* (2025). https://doi.org/10.1038/s41591-025-03494-0
58 Mi, H. & Thomas, P. PANTHER pathway: an ontology-based pathway database coupled with data analysis tools. *Methods Mol Biol* **563**, 123-140 (2009). https://doi.org/10.1007/978-1-60761-175-2_7
59 Tong, M., Jun, T., Nie, Y., Hao, J. & Fan, D. The Role of the Slit/Robo Signaling Pathway. *J Cancer* **10**, 2694-2705 (2019). https://doi.org/10.7150/jca.31877
60 Ho, D. M., Artavanis-Tsakonas, S. & Louvi, A. The Notch pathway in CNS homeostasis and neurodegeneration. *Wiley Interdiscip Rev Dev Biol* **9**, e358 (2020). https://doi.org/10.1002/wdev.358
61 Kapoor, A. & Nation, D. A. Role of Notch signaling in neurovascular aging and Alzheimer's disease. *Seminars in Cell & Developmental Biology* **116** (2021). https://doi.org/10.1016/j.semcdb.2020.12.011
62 Cui, Y., Rolova, T. & Fagerholm, S. C. The role of integrins in brain health and neurodegenerative diseases. *Eur J Cell Biol* **103**, 151441 (2024). https://doi.org/10.1016/j.ejcb.2024.151441
63 George-Hyslop, P. H. S. & Petit, A. Molecular biology and genetics of Alzheimer's disease. *Comptes Rendus. Biologies* **328** (2005). https://doi.org/10.1016/j.crvi.2004.10.013
64 Hasegawa, H. *et al.* The FAM3 superfamily member ILEI ameliorates Alzheimer's disease-like pathology by destabilizing the penultimate amyloid-β precursor. *Nature Communications 2014 5:1* **5** (2014). https://doi.org/10.1038/ncomms4917
65 Nishimura, M. *et al.* FAM3C in Alzheimer's disease: a risk-related molecule and potential therapeutic target. *Genetics, Neurology, Behavior, and Diet in Dementia* (2020). https://doi.org/10.1016/B978-0-12-815868-5.00019-0
66 Miyazaki, Y. *et al.* Oligodendrocyte-derived LGI3 and its receptor ADAM23 organize juxtaparanodal Kv1 channel clustering for short-term synaptic plasticity. *Cell Rep* **43**, 113634 (2024). https://doi.org/10.1016/j.celrep.2023.113634
67 Meilandt, W. J. *et al.* Enkephalin elevations contribute to neuronal and behavioral impairments in a transgenic mouse model of Alzheimer's disease. *J Neurosci* **28**, 5007-5017 (2008). https://doi.org/10.1523/jneurosci.0590-08.2008
68 Wei, J. *et al.* Reduced HGF/MET Signaling May Contribute to the Synaptic Pathology in an Alzheimer's Disease Mouse Model. *Front Aging Neurosci* **14**, 954266 (2022). https://doi.org/10.3389/fnagi.2022.954266
69 Ibrahim, A. M. *et al.* Brain-Derived Neurotropic Factor in Neurodegenerative Disorders. *Biomedicines* **10** (2022). https://doi.org/10.3390/biomedicines10051143
70 Gao, L. *et al.* Brain-derived neurotrophic factor in Alzheimer's disease and its pharmaceutical potential. *Translational Neurodegeneration 2022 11:1* **11** (2022-01-28). https://doi.org/10.1186/s40035-022-00279-0
71 Warth Perez Arias, C. C. *et al.* Proteomic analysis of the human hippocampus identifies neuronal pentraxin 1 (NPTX1) as synapto□axonal target in late□stage Parkinson's disease. *Journal of Neurochemistry* **166** (2023). https://doi.org/10.1111/jnc.15924
72 Gómez de San José, N. *et al.* Neuronal pentraxins as biomarkers of synaptic activity: from physiological functions to pathological changes in neurodegeneration. *Journal of Neural Transmission 2021 129:2* **129** (2021). https://doi.org/10.1007/s00702-021-02411-2
73 Nilsson, J. *et al.* Cerebrospinal Fluid Biomarkers of Synaptic Dysfunction are Altered in Parkinson's Disease and Related Disorders. *Mov Disord* **38**, 267-277 (2023). https://doi.org/10.1002/mds.29287
74 Zhang, B. *et al.* Integrated systems approach identifies genetic nodes and networks in late-onset Alzheimer's disease. *Cell* **153**, 707-720 (2013). https://doi.org/10.1016/j.cell.2013.03.030

75 Seppälä, E. H. *et al.* LGI2 truncation causes a remitting focal epilepsy in dogs. *PLoS Genet* **7**, e1002194 (2011). https://doi.org/10.1371/journal.pgen.1002194
76 Kozar-Gillan, N. *et al.* LGI3/2–ADAM23 interactions cluster Kv1 channels in myelinated axons to regulate refractory period. *Journal of Cell Biology* **222** (2023/04/03). https://doi.org/10.1083/jcb.202211031
77 Kegel, L., Aunin, E., Meijer, D. & Bermingham, J. R. LGI proteins in the nervous system. *ASN Neuro* **5**, 167-181 (2013). https://doi.org/10.1042/an20120095
78 Abad, M. A., Enguita, M., DeGregorio-Rocasolano, N., Ferrer, I. & Trullas, R. Neuronal pentraxin 1 contributes to the neuronal damage evoked by amyloid-beta and is overexpressed in dystrophic neurites in Alzheimer's brain. *J Neurosci* **26**, 12735-12747 (2006). https://doi.org/10.1523/jneurosci.0575-06.2006
79 Lewandowski, C. T., Laham, M. S. & Thatcher, G. R. J. Remembering your A, B, C's: Alzheimer's disease and ABCA1. *Acta Pharm Sin B* **12**, 995-1018 (2022). https://doi.org/10.1016/j.apsb.2022.01.011
80 Siletti, K. *et al.* Transcriptomic diversity of cell types across the adult human brain. *Science* **382**, eadd7046 (2023). https://doi.org/10.1126/science.add7046
81 Ding, S. L. *et al.* Comprehensive cellular-resolution atlas of the adult human brain. *J Comp Neurol* **524**, 3127-3481 (2016). https://doi.org/10.1002/cne.24080
82 Hutton, M. & Hardy, J. The Presenilins and Alzheimer's Disease. *Human Molecular Genetics* **6** (1997). https://doi.org/10.1093/hmg/6.10.1639
83 Nanclares, C., Baraibar, A. M., Araque, A. & Kofuji, P. Dysregulation of Astrocyte-Neuronal Communication in Alzheimer's Disease. *Int J Mol Sci* **22** (2021). https://doi.org/10.3390/ijms22157887
84 Nam, M.-H. *et al.* Visualizing reactive astrocyte-neuron interaction in Alzheimer's disease using 11C-acetate and 18F-FDG. *Brain* **146** (2023). https://doi.org/10.1093/brain/awad037
85 Liu, A., Fernandes, B. S., Citu, C. & Zhao, Z. Unraveling the intercellular communication disruption and key pathways in Alzheimer's disease: an integrative study of single-nucleus transcriptomes and genetic association. *Alzheimers Res Ther* **16**, 3 (2024). https://doi.org/10.1186/s13195-023-01372-w
86 Bartas, K. *et al.* Analysis of changes in inter-cellular communications during Alzheimer's Disease pathogenesis reveals conserved changes in glutamatergic transmission in mice and humans. *bioRxiv* (2024). https://doi.org/10.1101/2024.04.30.591802
87 Mathys, H. *et al.* Single-cell multiregion dissection of Alzheimer's disease. *Nature* **632**, 858-868 (2024). https://doi.org/10.1038/s41586-024-07606-7
88 Pak, V. *et al.* Distinctive whole-brain cell types predict tissue damage patterns in thirteen neurodegenerative conditions. *Elife* **12** (2024). https://doi.org/10.7554/eLife.89368
89 Soelter, T. M., Howton, T. C., Clark, A. D., Oza, V. H. & Lasseigne, B. N. Altered glia-neuron communication in Alzheimer's Disease affects WNT, p53, and NFkB Signaling determined by snRNA-seq. *Cell Commun Signal* **22**, 317 (2024). https://doi.org/10.1186/s12964-024-01686-8
90 Talairach, J. & Szikla, G. Application of stereotactic concepts to the surgery of epilepsy. *Acta Neurochir Suppl (Wien)* **30**, 35-54 (1980). https://doi.org/10.1007/978-3-7091-8592-6_5
91 Hou, R., Denisenko, E., Ong, H. T., Ramilowski, J. A. & Forrest, A. R. R. Predicting cell-to-cell communication networks using NATMI. *Nat Commun* **11**, 5011 (2020). https://doi.org/10.1038/s41467-020-18873-z
92 Browaeys, R., Saelens, W. & Saeys, Y. NicheNet: modeling intercellular communication by linking ligands to target genes. *Nat Methods* **17**, 159-162 (2020). https://doi.org/10.1038/s41592-019-0667-5
93 Dimitrov, D. *et al.* Comparison of methods and resources for cell-cell communication inference from single-cell RNA-Seq data. *Nat Commun* **13**, 3224 (2022). https://doi.org/10.1038/s41467-022-30755-0

94 Jin, S. *et al.* Inference and analysis of cell-cell communication using CellChat. *Nat Commun* **12**, 1088 (2021). https://doi.org/10.1038/s41467-021-21246-9
95 Cabello-Aguilar, S. *et al.* SingleCellSignalR: inference of intercellular networks from single-cell transcriptomics. *Nucleic Acids Res* **48**, e55 (2020). https://doi.org/10.1093/nar/gkaa183
96 Noel, F. *et al.* Dissection of intercellular communication using the transcriptome-based framework ICELLNET. *Nat Commun* **12**, 1089 (2021). https://doi.org/10.1038/s41467-021-21244-x
97 Wang, Y. *et al.* iTALK: an R Package to Characterize and Illustrate Intercellular Communication. *bioRxiv* (2019). https://doi.org/10.1101/507871
98 Shao, X. *et al.* CellTalkDB: a manually curated database of ligand-receptor interactions in humans and mice. *Brief Bioinform* **22** (2021). https://doi.org/10.1093/bib/bbaa269
99 Zhao, W., Johnston, K. G., Ren, H., Xu, X. & Nie, Q. Inferring neuron-neuron communications from single-cell transcriptomics through NeuronChat. *Nat Commun* **14**, 1128 (2023). https://doi.org/10.1038/s41467-023-36800-w
100 Seidlitz, J. *et al.* Transcriptomic and cellular decoding of regional brain vulnerability to neurogenetic disorders. *Nat Commun* **11**, 3358 (2020). https://doi.org/10.1038/s41467-020-17051-5
101 Türei, D. *et al.* Integrated intra- and intercellular signaling knowledge for multicellular omics analysis. *Mol Syst Biol* **17**, e9923 (2021). https://doi.org/10.15252/msb.20209923
102 Badia-i-Mompel, P. *et al.* decoupleR: ensemble of computational methods to infer biological activities from omics data. *Bioinformatics Advances* **2** (2022). https://doi.org/10.1093/bioadv/vbac016
103 Efremova, M., Vento-Tormo, M., Teichmann, S. A. & Vento-Tormo, R. CellPhoneDB: inferring cell-cell communication from combined expression of multi-subunit ligand-receptor complexes. *Nat Protoc* **15**, 1484-1506 (2020). https://doi.org/10.1038/s41596-020-0292-x
104 Raredon, M. S. B. *et al.* Computation and visualization of cell-cell signaling topologies in single-cell systems data using Connectome. *Sci Rep* **12**, 4187 (2022). https://doi.org/10.1038/s41598-022-07959-x
105 Boeve, B. F., Boxer, A. L., Kumfor, F., Pijnenburg, Y. & Rohrer, J. D. Advances and controversies in frontotemporal dementia: diagnosis, biomarkers, and therapeutic considerations. *Lancet Neurol* **21**, 258-272 (2022). https://doi.org/10.1016/s1474-4422(21)00341-0
106 Ashburner, J. & Friston, K. J. Voxel-based morphometry--the methods. *Neuroimage* **11**, 805-821 (2000). https://doi.org/10.1006/nimg.2000.0582
107 Aubert-Broche, B. *et al.* A new method for structural volume analysis of longitudinal brain MRI data and its application in studying the growth trajectories of anatomical brain structures in childhood. *Neuroimage* **82**, 393-402 (2013). https://doi.org/10.1016/j.neuroimage.2013.05.065
108 Parkinson Progression Marker, I. The Parkinson Progression Marker Initiative (PPMI). *Prog Neurobiol* **95**, 629-635 (2011). https://doi.org/10.1016/j.pneurobio.2011.09.005
109 Kalra, S. *et al.* (medRxiv, 2020).
110 Brooks, B. R., Miller, R. G., Swash, M. & Munsat, T. L. El Escorial revisited: revised criteria for the diagnosis of amyotrophic lateral sclerosis. *Amyotroph Lateral Scler Other Motor Neuron Disord* **1**, 293-299 (2000). https://doi.org/10.1080/146608200300079536
111 Staffaroni, A. M. *et al.* Longitudinal multimodal imaging and clinical endpoints for frontotemporal dementia clinical trials. *Brain* **142**, 443-459 (2019). https://doi.org/10.1093/brain/awy319
112 Neary, D. *et al.* Frontotemporal lobar degeneration: a consensus on clinical diagnostic criteria. *Neurology* **51**, 1546-1554 (1998). https://doi.org/10.1212/wnl.51.6.1546
113 Rascovsky, K. *et al.* Sensitivity of revised diagnostic criteria for the behavioural variant of frontotemporal dementia. *Brain* **134**, 2456-2477 (2011). https://doi.org/10.1093/brain/awr179
114 Gorno-Tempini, M. L. *et al.* Classification of primary progressive aphasia and its variants. *Neurology* **76**, 1006-1014 (2011). https://doi.org/10.1212/WNL.0b013e31821103e6

115 Lin, S. J. *et al.* Neuroimaging signatures predicting motor improvement to focused ultrasound subthalamotomy in Parkinson's disease. *NPJ Parkinsons Dis* **8**, 70 (2022). https://doi.org/10.1038/s41531-022-00332-9

116 McIntosh, A. R. & Lobaugh, N. J. Partial least squares analysis of neuroimaging data: applications and advances. *Neuroimage* **23 Suppl 1**, S250-263 (2004). https://doi.org/10.1016/j.neuroimage.2004.07.020

117 Geladi, P. & Kowalski, B. R. Partial least-squares regression: a tutorial. *Analytica Chimica Acta* **185**, 1-17 (1986). https://doi.org/https://doi.org/10.1016/0003-2670(86)80028-9

118 Ge, S. X., Jung, D. & Yao, R. ShinyGO: a graphical gene-set enrichment tool for animals and plants. *Bioinformatics* **36**, 2628-2629 (2020). https://doi.org/10.1093/bioinformatics/btz931

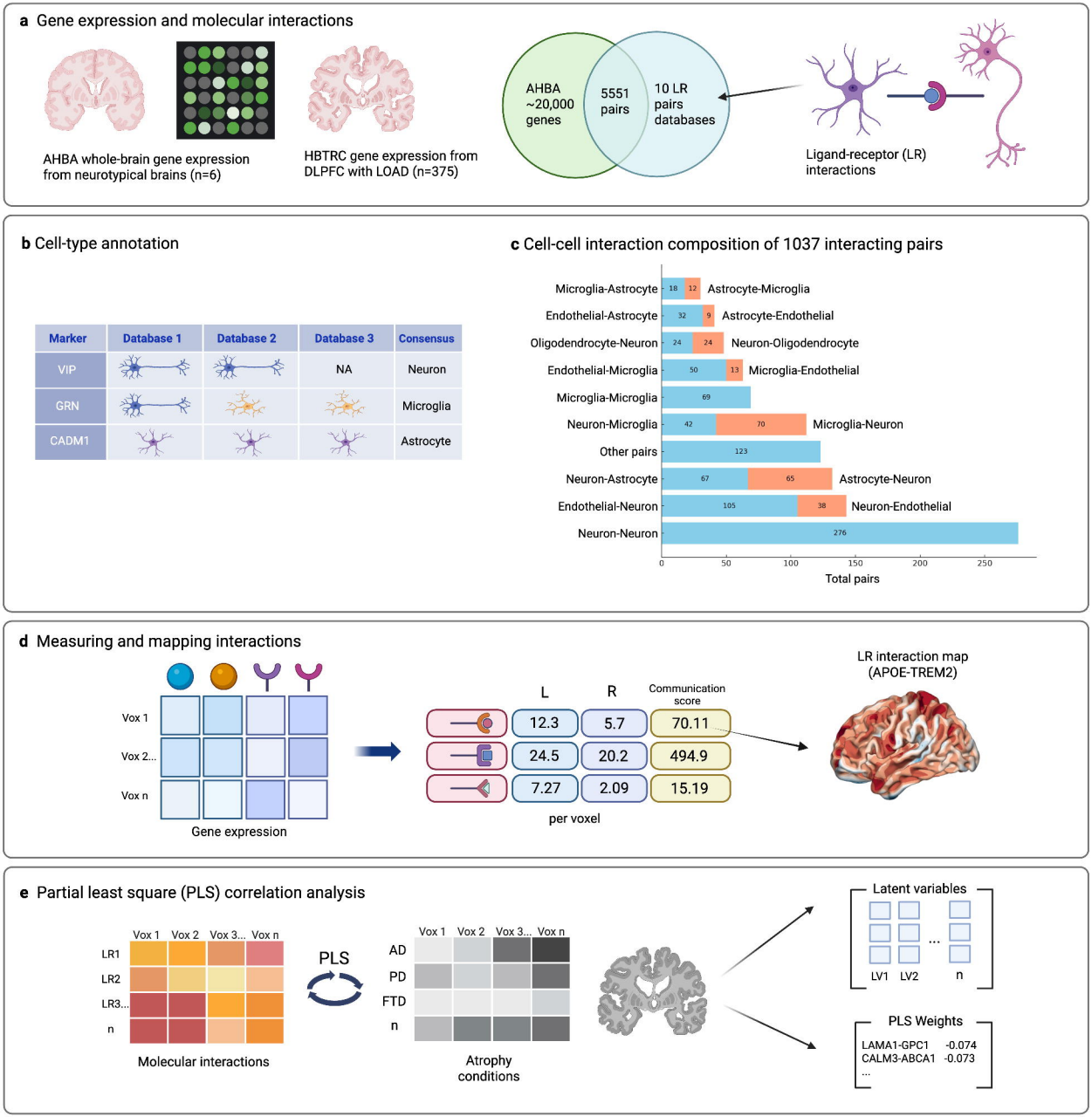
a Gene expression and molecular interactions
AHBA whole-brain gene expression from neurotypical brains (n=6)
HBTRC gene expression from DLPFC with LOAD (n=375)
AHBA ~20,000 genes
5551 pairs
10 LR pairs databases
Ligand-receptor (LR) interactions
b Cell-type annotation
Marker
Database 1
Database 2
Database 3
Consensus
VIP
NA
Neuron
GRN
Microglia
CADM1
Astrocyte
c Cell-cell interaction composition of 1037 interacting pairs
Microglia-Astrocyte 18 12 Astrocyte-Microglia
Endothelial-Astrocyte 32 9 Astrocyte-Endothelial
Oligodendrocyte-Neuron 24 24 Neuron-Oligodendrocyte
Endothelial-Microglia 50 13 Microglia-Endothelial
Microglia-Microglia 69
Neuron-Microglia 42 70 Microglia-Neuron
Other pairs 123
Neuron-Astrocyte 67 65 Astrocyte-Neuron
Endothelial-Neuron 105 38 Neuron-Endothelial
Neuron-Neuron 276
0 50 100 150 200 250
Total pairs
d Measuring and mapping interactions
Vox 1
Vox 2...
Vox n
Gene expression
L
R
Communication score
12.3 5.7 70.11
24.5 20.2 494.9
7.27 2.09 15.19
per voxel
LR interaction map (APOE-TREM2)
e Partial least square (PLS) correlation analysis
Vox 1 Vox 2 Vox 3... Vox n
LR1
LR2
LR3...
n
Molecular interactions
PLS
AD
PD
FTD
n
Atrophy conditions
Latent variables
LV1 LV2 ... n
PLS Weights
LAMA1-GPC1 -0.074
CALM3-ABCA1 -0.073
...

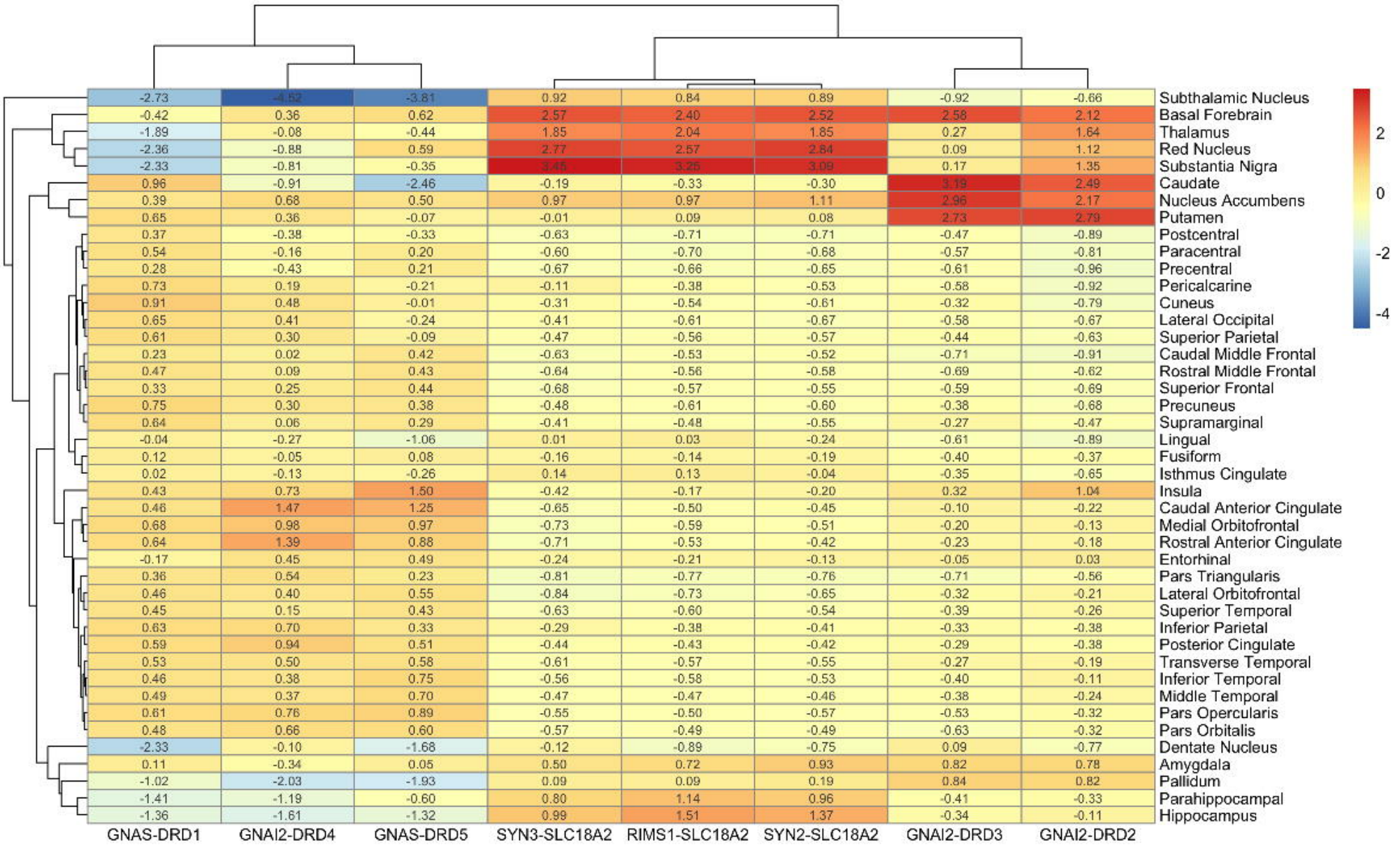
GNAS-DRD1
GNAI2-DRD4
GNAS-DRD5
SYN3-SLC18A2
RIMS1-SLC18A2
SYN2-SLC18A2
GNAI2-DRD3
GNAI2-DRD2
Subthalamic Nucleus -2.73 -4.52 -3.81 0.92 0.84 0.89 -0.92 -0.66
Basal Forebrain -0.42 0.36 0.62 2.57 2.40 2.52 2.58 2.12
Thalamus -1.89 -0.08 -0.44 1.85 2.04 1.85 0.27 1.64
Red Nucleus -2.36 -0.88 0.59 2.77 2.57 2.84 0.09 1.12
Substantia Nigra -2.33 -0.81 -0.35 3.45 3.26 3.09 0.17 1.35
Caudate 0.96 -0.91 -2.46 -0.19 -0.33 -0.30 3.19 2.49
Nucleus Accumbens 0.39 0.68 0.50 0.97 0.97 1.11 2.96 2.17
Putamen 0.65 0.36 -0.07 -0.01 0.09 0.08 2.73 2.79
Postcentral 0.37 -0.38 -0.33 -0.63 -0.71 -0.71 -0.47 -0.89
Paracentral 0.54 -0.16 0.20 -0.60 -0.70 -0.68 -0.57 -0.81
Precentral 0.28 -0.43 0.21 -0.67 -0.66 -0.65 -0.61 -0.96
Pericalcarine 0.73 0.19 -0.21 -0.11 -0.38 -0.53 -0.58 -0.92
Cuneus 0.91 0.48 -0.01 -0.31 -0.54 -0.61 -0.32 -0.79
Lateral Occipital 0.65 0.41 -0.24 -0.41 -0.61 -0.67 -0.58 -0.67
Superior Parietal 0.61 0.30 -0.09 -0.47 -0.56 -0.57 -0.44 -0.63
Caudal Middle Frontal 0.23 0.02 0.42 -0.63 -0.53 -0.52 -0.71 -0.91
Rostral Middle Frontal 0.47 0.09 0.43 -0.64 -0.56 -0.58 -0.69 -0.62
Superior Frontal 0.33 0.25 0.44 -0.68 -0.57 -0.55 -0.59 -0.69
Precuneus 0.75 0.30 0.38 -0.48 -0.61 -0.60 -0.38 -0.68
Supramarginal 0.64 0.06 0.29 -0.41 -0.48 -0.55 -0.27 -0.47
Lingual -0.04 -0.27 -1.06 0.01 0.03 -0.24 -0.61 -0.89
Fusiform 0.12 -0.05 0.08 -0.16 -0.14 -0.19 -0.40 -0.37
Isthmus Cingulate 0.02 -0.13 -0.26 0.14 0.13 -0.04 -0.35 -0.65
Insula 0.43 0.73 1.50 -0.42 -0.17 -0.20 0.32 1.04
Caudal Anterior Cingulate 0.46 1.47 1.25 -0.65 -0.50 -0.45 -0.10 -0.22
Medial Orbitofrontal 0.68 0.98 0.97 -0.73 -0.59 -0.51 -0.20 -0.13
Rostral Anterior Cingulate 0.64 1.39 0.88 -0.71 -0.53 -0.42 -0.23 -0.18
Entorhinal -0.17 0.45 0.49 -0.24 -0.21 -0.13 -0.05 0.03
Pars Triangularis 0.36 0.54 0.23 -0.81 -0.77 -0.76 -0.71 -0.56
Lateral Orbitofrontal 0.46 0.40 0.55 -0.84 -0.73 -0.65 -0.32 -0.21
Superior Temporal 0.45 0.15 0.43 -0.63 -0.60 -0.54 -0.39 -0.26
Inferior Parietal 0.63 0.70 0.33 -0.29 -0.38 -0.41 -0.33 -0.38
Posterior Cingulate 0.59 0.94 0.51 -0.44 -0.43 -0.42 -0.29 -0.38
Transverse Temporal 0.53 0.50 0.58 -0.61 -0.57 -0.55 -0.27 -0.19
Inferior Temporal 0.46 0.38 0.75 -0.56 -0.58 -0.53 -0.40 -0.11
Middle Temporal 0.49 0.37 0.70 -0.47 -0.47 -0.46 -0.38 -0.24
Pars Opercularis 0.61 0.76 0.89 -0.55 -0.50 -0.57 -0.53 -0.32
Pars Orbitalis 0.48 0.66 0.60 -0.57 -0.49 -0.49 -0.63 -0.32
Dentate Nucleus -2.33 -0.10 -1.68 -0.12 -0.89 -0.75 0.09 -0.77
Amygdala 0.11 -0.34 0.05 0.50 0.72 0.93 0.82 0.78
Pallidum -1.02 -2.03 -1.93 0.09 0.09 0.19 0.84 0.82
Parahippocampal -1.41 -1.19 -0.60 0.80 1.14 0.96 -0.41 -0.33
Hippocampus -1.36 -1.61 -1.32 0.99 1.51 1.37 -0.34 -0.11
2
0
-2
-4

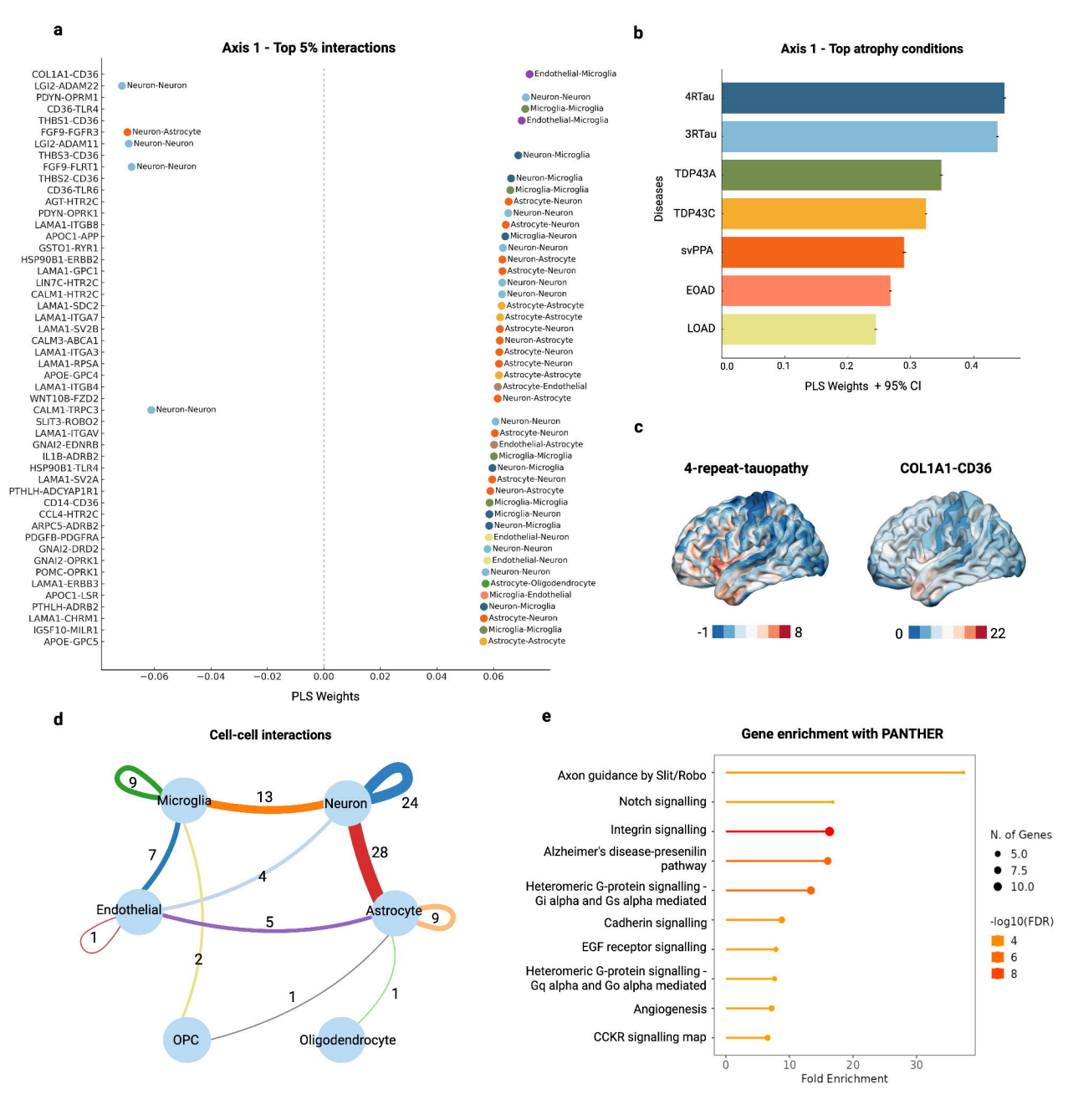
a
Axis 1 - Top 5% interactions
COL1A1-CD36
LGI2-ADAM22
PDYN-OPRM1
CD36-TLR4
THBS1-CD36
FGF9-FGFR3
LGI2-ADAM11
THBS3-CD36
FGF9-FLRT1
THBS2-CD36
CD36-TLR6
AGT-HTR2C
PDYN-OPRK1
LAMA1-ITGB8
APOC1-APP
GSTO1-RYR1
HSP90B1-ERBB2
LAMA1-GPC1
LIN7C-HTR2C
CALM1-HTR2C
LAMA1-SDC2
LAMA1-ITGA7
LAMA1-SV2B
CALM3-ABCA1
LAMA1-ITGA3
LAMA1-RPSA
APOE-GPC4
LAMA1-ITGB4
WNT10B-FZD2
CALM1-TRPC3
SLIT3-ROBO2
LAMA1-ITGAV
GNAI2-EDNRB
IL1B-ADRB2
HSP90B1-TLR4
LAMA1-SV2A
PTHLH-ADCYAP1R1
CD14-CD36
CCL4-HTR2C
ARPC5-ADRB2
PDGFB-PDGFRA
GNAI2-DRD2
GNAI2-OPRK1
POMC-OPRK1
LAMA1-ERBB3
APOC1-LSR
PTHLH-ADRB2
LAMA1-CHRM1
IGSF10-MILR1
APOE-GPC5
Neuron-Neuron
Neuron-Astrocyte
Neuron-Neuron
Neuron-Neuron
Neuron-Neuron
Endothelial-Microglia
Neuron-Neuron
Microglia-Microglia
Endothelial-Microglia
Neuron-Microglia
Neuron-Microglia
Microglia-Microglia
Astrocyte-Neuron
Neuron-Neuron
Astrocyte-Neuron
Microglia-Neuron
Neuron-Neuron
Neuron-Astrocyte
Astrocyte-Neuron
Neuron-Neuron
Neuron-Neuron
Astrocyte-Astrocyte
Astrocyte-Astrocyte
Astrocyte-Neuron
Neuron-Astrocyte
Astrocyte-Neuron
Astrocyte-Neuron
Astrocyte-Astrocyte
Astrocyte-Endothelial
Neuron-Astrocyte
Neuron-Neuron
Astrocyte-Neuron
Endothelial-Astrocyte
Microglia-Microglia
Neuron-Microglia
Astrocyte-Neuron
Neuron-Astrocyte
Microglia-Microglia
Microglia-Neuron
Neuron-Microglia
Endothelial-Neuron
Neuron-Neuron
Endothelial-Neuron
Neuron-Neuron
Astrocyte-Oligodendrocyte
Microglia-Endothelial
Neuron-Microglia
Astrocyte-Neuron
Microglia-Microglia
Astrocyte-Astrocyte
−0.06
−0.04
−0.02
0.00
0.02
0.04
0.06
PLS Weights
b
Axis 1 - Top atrophy conditions
Diseases
4RTau
3RTau
TDP43A
TDP43C
svPPA
EOAD
LOAD
0.0
0.1
0.2
0.3
0.4
PLS Weights + 95% CI
c
4-repeat-tauopathy
COL1A1-CD36
-1
8
0
22
d
Cell-cell interactions
Microglia
Neuron
Endothelial
Astrocyte
OPC
Oligodendrocyte
9
13
24
7
28
4
5
9
1
2
1
1
e
Gene enrichment with PANTHER
Axon guidance by Slit/Robo
Notch signalling
Integrin signalling
Alzheimer's disease-presenilin pathway
Heteromeric G-protein signalling - Gi alpha and Gs alpha mediated
Cadherin signalling
EGF receptor signalling
Heteromeric G-protein signalling - Gq alpha and Go alpha mediated
Angiogenesis
CCKR signalling map
0
10
20
30
Fold Enrichment
N. of Genes
5.0
7.5
10.0
-log10(FDR)
4
6
8

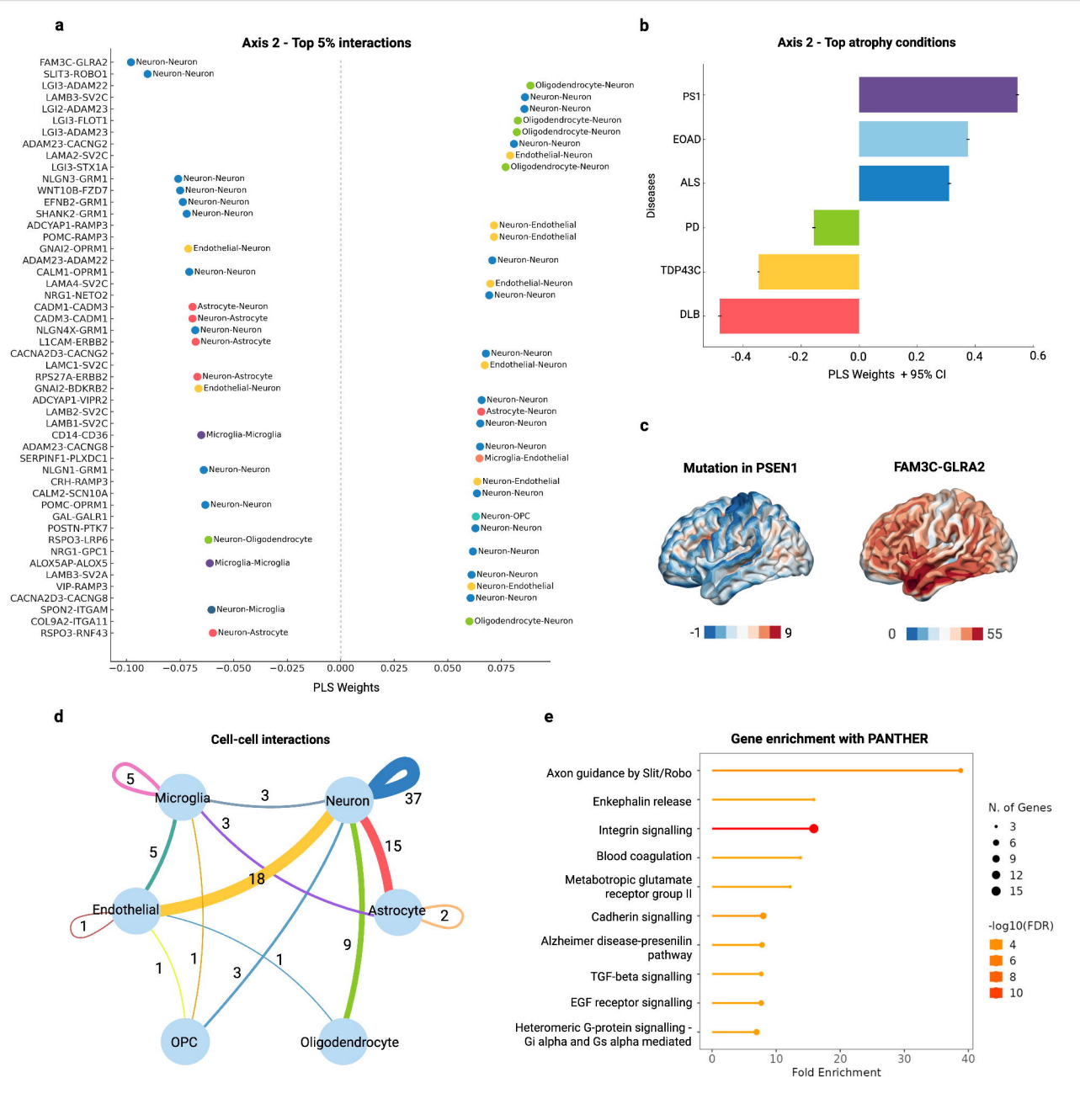
a
Axis 2 - Top 5% interactions
FAM3C-GLRA2
SLIT3-ROBO1
LGI3-ADAM22
LAMB3-SV2C
LGI2-ADAM23
LGI3-FLOT1
LGI3-ADAM23
ADAM23-CACNG2
LAMA2-SV2C
LGI3-STX1A
NLGN3-GRM1
WNT10B-FZD7
EFNB2-GRM1
SHANK2-GRM1
ADCYAP1-RAMP3
POMC-RAMP3
GNAI2-OPRM1
ADAM23-ADAM22
CALM1-OPRM1
LAMA4-SV2C
NRG1-NETO2
CADM1-CADM3
CADM3-CADM1
NLGN4X-GRM1
L1CAM-ERBB2
CACNA2D3-CACNG2
LAMC1-SV2C
RPS27A-ERBB2
GNAI2-BDKRB2
ADCYAP1-VIPR2
LAMB2-SV2C
LAMB1-SV2C
CD14-CD36
ADAM23-CACNG8
SERPINF1-PLXDC1
NLGN1-GRM1
CRH-RAMP3
CALM2-SCN10A
POMC-OPRM1
GAL-GALR1
POSTN-PTK7
RSPO3-LRP6
NRG1-GPC1
ALOX5AP-ALOX5
LAMB3-SV2A
VIP-RAMP3
CACNA2D3-CACNG8
SPON2-ITGAM
COL9A2-ITGA11
RSPO3-RNF43
Neuron-Neuron
Neuron-Neuron
Oligodendrocyte-Neuron
Neuron-Neuron
Neuron-Neuron
Oligodendrocyte-Neuron
Oligodendrocyte-Neuron
Neuron-Neuron
Endothelial-Neuron
Oligodendrocyte-Neuron
Neuron-Neuron
Neuron-Neuron
Neuron-Neuron
Neuron-Neuron
Neuron-Endothelial
Neuron-Endothelial
Endothelial-Neuron
Neuron-Neuron
Neuron-Neuron
Endothelial-Neuron
Neuron-Neuron
Astrocyte-Neuron
Neuron-Astrocyte
Neuron-Neuron
Neuron-Astrocyte
Neuron-Neuron
Endothelial-Neuron
Neuron-Astrocyte
Endothelial-Neuron
Neuron-Neuron
Astrocyte-Neuron
Neuron-Neuron
Microglia-Microglia
Neuron-Neuron
Microglia-Endothelial
Neuron-Neuron
Neuron-Endothelial
Neuron-Neuron
Neuron-Neuron
Neuron-OPC
Neuron-Neuron
Neuron-Oligodendrocyte
Microglia-Microglia
Neuron-Neuron
Neuron-Neuron
Neuron-Endothelial
Neuron-Neuron
Neuron-Microglia
Oligodendrocyte-Neuron
Neuron-Astrocyte
−0.100
−0.075
−0.050
−0.025
0.000
0.025
0.050
0.075
PLS Weights
b
Axis 2 - Top atrophy conditions
Diseases
PS1
EOAD
ALS
PD
TDP43C
DLB
-0.4
-0.2
0.0
0.2
0.4
0.6
PLS Weights + 95% CI
c
Mutation in PSEN1
FAM3C-GLRA2
-1
9
0
55
d
Cell-cell interactions
Microglia
Neuron
Endothelial
Astrocyte
OPC
Oligodendrocyte
5
3
37
3
5
15
18
2
1
9
1
1
3
1
e
Gene enrichment with PANTHER
Axon guidance by Slit/Robo
Enkephalin release
Integrin signalling
Blood coagulation
Metabotropic glutamate receptor group II
Cadherin signalling
Alzheimer disease-presenilin pathway
TGF-beta signalling
EGF receptor signalling
Heteromeric G-protein signalling - Gi alpha and Gs alpha mediated
0
10
20
30
40
Fold Enrichment
N. of Genes
3
6
9
12
15
-log10(FDR)
4
6
8
10

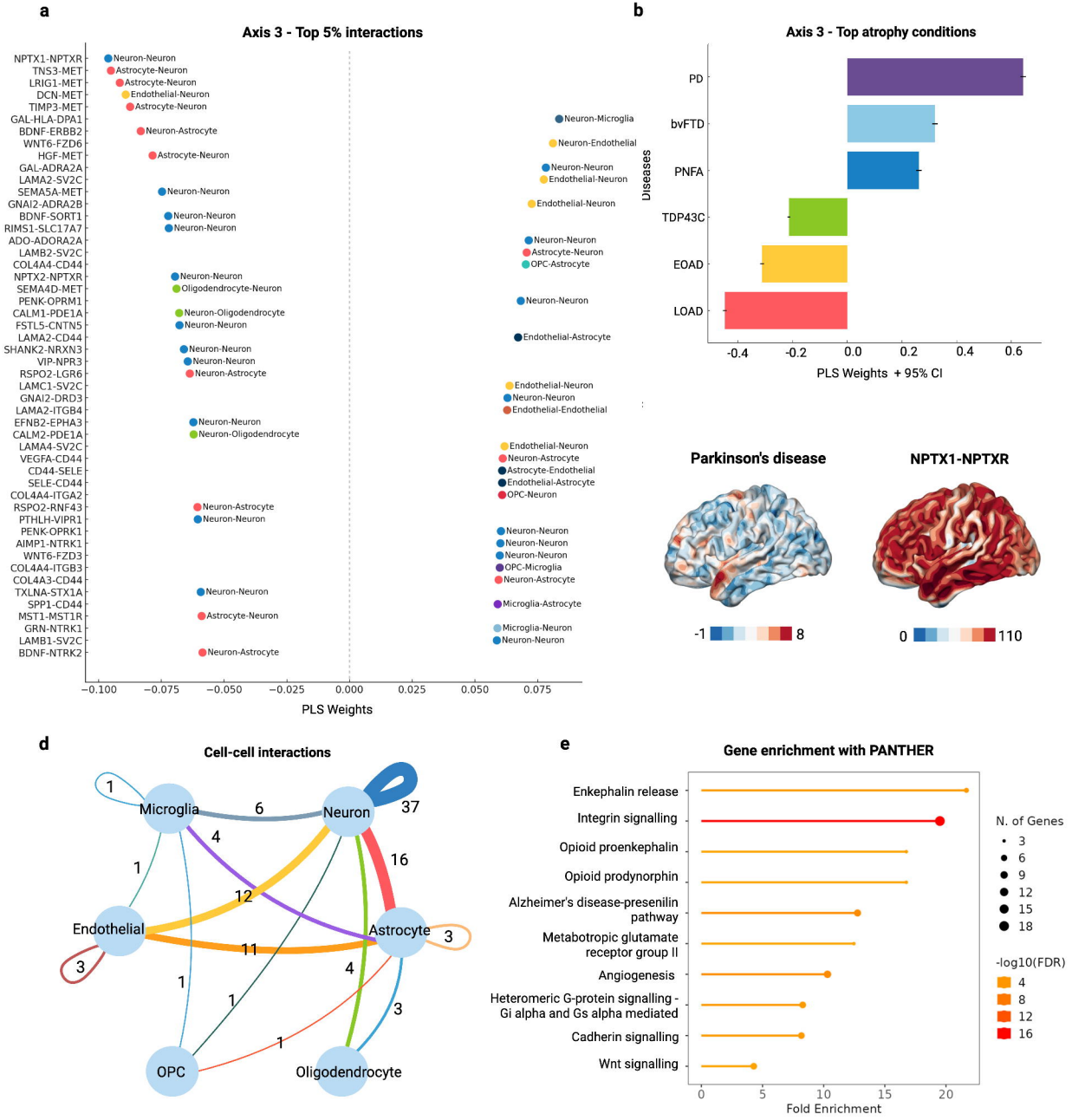
a
Axis 3 - Top 5% interactions
NPTX1-NPTXR
TNS3-MET
LRIG1-MET
DCN-MET
TIMP3-MET
GAL-HLA-DPA1
BDNF-ERBB2
WNT6-FZD6
HGF-MET
GAL-ADRA2A
LAMA2-SV2C
SEMA5A-MET
GNAI2-ADRA2B
BDNF-SORT1
RIMS1-SLC17A7
ADO-ADORA2A
LAMB2-SV2C
COL4A4-CD44
NPTX2-NPTXR
SEMA4D-MET
PENK-OPRM1
CALM1-PDE1A
FSTL5-CNTN5
LAMA2-CD44
SHANK2-NRXN3
VIP-NPR3
RSPO2-LGR6
LAMC1-SV2C
GNAI2-DRD3
LAMA2-ITGB4
EFNB2-EPHA3
CALM2-PDE1A
LAMA4-SV2C
VEGFA-CD44
CD44-SELE
SELE-CD44
COL4A4-ITGA2
RSPO2-RNF43
PTHLH-VIPR1
PENK-OPRK1
AIMP1-NTRK1
WNT6-FZD3
COL4A4-ITGB3
COL4A3-CD44
TXLNA-STX1A
SPP1-CD44
MST1-MST1R
GRN-NTRK1
LAMB1-SV2C
BDNF-NTRK2
Neuron-Neuron
Astrocyte-Neuron
Astrocyte-Neuron
Endothelial-Neuron
Astrocyte-Neuron
Neuron-Astrocyte
Astrocyte-Neuron
Neuron-Neuron
Neuron-Neuron
Neuron-Neuron
Neuron-Neuron
Oligodendrocyte-Neuron
Neuron-Oligodendrocyte
Neuron-Neuron
Neuron-Neuron
Neuron-Neuron
Neuron-Astrocyte
Neuron-Neuron
Neuron-Oligodendrocyte
Neuron-Astrocyte
Neuron-Neuron
Neuron-Neuron
Astrocyte-Neuron
Neuron-Astrocyte
−0.100
−0.075
−0.050
−0.025
0.000
0.025
0.050
0.075
PLS Weights
Neuron-Microglia
Neuron-Endothelial
Neuron-Neuron
Endothelial-Neuron
Endothelial-Neuron
Neuron-Neuron
Astrocyte-Neuron
OPC-Astrocyte
Neuron-Neuron
Endothelial-Astrocyte
Endothelial-Neuron
Neuron-Neuron
Endothelial-Endothelial
Endothelial-Neuron
Neuron-Astrocyte
Astrocyte-Endothelial
Endothelial-Astrocyte
OPC-Neuron
Neuron-Neuron
Neuron-Neuron
Neuron-Neuron
OPC-Microglia
Neuron-Astrocyte
Microglia-Astrocyte
Microglia-Neuron
Neuron-Neuron
b
Axis 3 - Top atrophy conditions
Diseases
PD
bvFTD
PNFA
TDP43C
EOAD
LOAD
-0.4
-0.2
0.0
0.2
0.4
0.6
PLS Weights + 95% CI
Parkinson's disease
NPTX1-NPTXR
-1
8
0
110
d
Cell-cell interactions
Microglia
Neuron
Endothelial
Astrocyte
OPC
Oligodendrocyte
1
6
37
4
16
1
12
11
3
3
1
4
1
3
1
e
Gene enrichment with PANTHER
Enkephalin release
Integrin signalling
Opioid proenkephalin
Opioid prodynorphin
Alzheimer's disease-presenilin pathway
Metabotropic glutamate receptor group II
Angiogenesis
Heteromeric G-protein signalling - Gi alpha and Gs alpha mediated
Cadherin signalling
Wnt signalling
0
5
10
15
20
Fold Enrichment
N. of Genes
3
6
9
12
15
18
-log10(FDR)
4
8
12
16

a

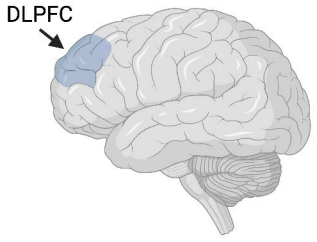

Late Onset Alzheimer's Disease (LOAD)

Top 10 interactions

HBTRC	AHBA
CALM3-ADCY8	LGI2-ADAM22
LGI2-ADAM23	THBS1-CD36
CALM2-ADCY8	THBS3-CD36
CALM3-ABCA1	CD36-TLR4
LGI4-ADAM23	LGI2-ADAM11
CALM3-KCNQ3	FGF9-FLRT1
ENTPD1-ADORA2A	SEMA4F-NRP2
LGI2-ADAM11	COL1A1-CD36
F8-LRP4	CD14-CD36
LAMA1-ITGB8	NRG1-GPC1

Atrophy map for LOAD

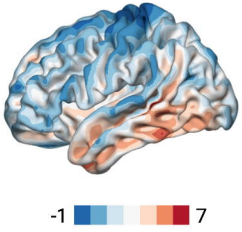

b

Overlapping interactions

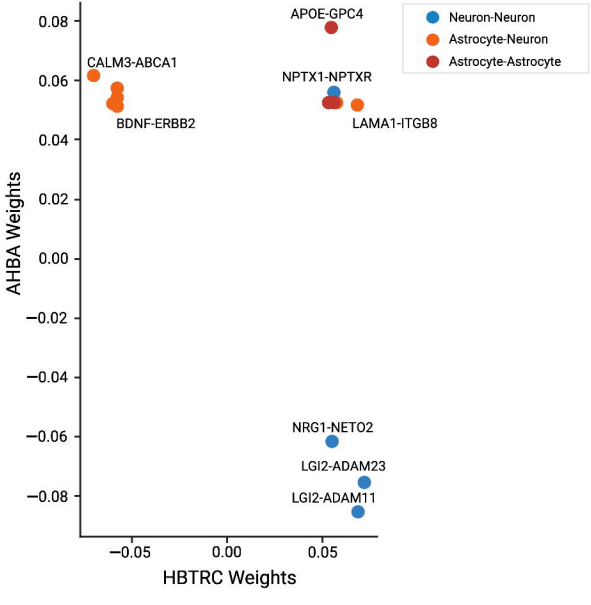

c

Cell-cell interactions

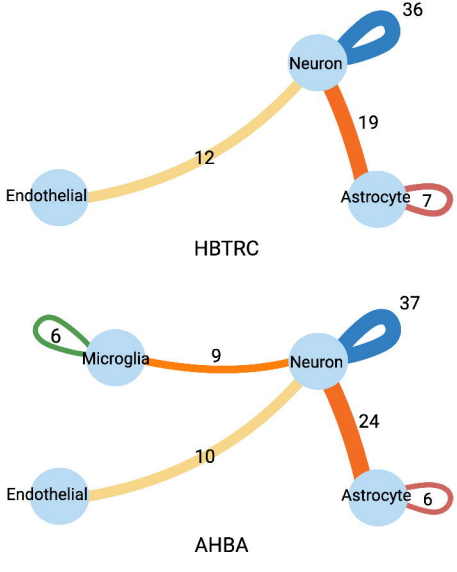

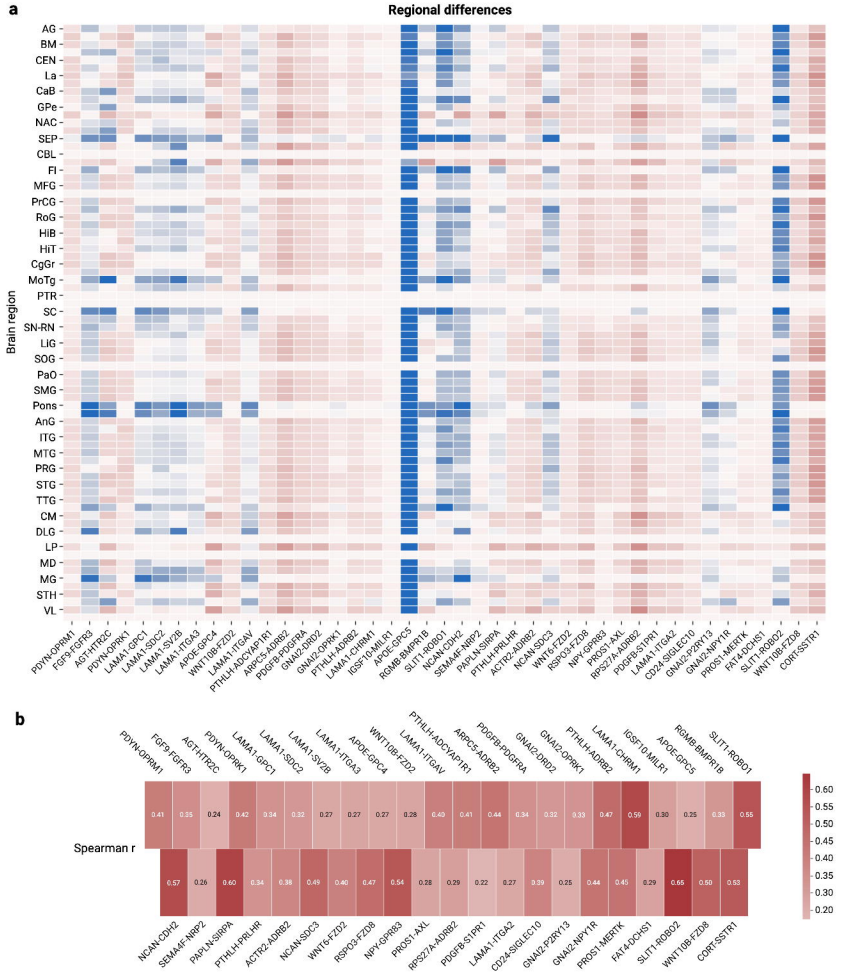
a
Regional differences
Brain region
AG
BM
CEN
La
CaB
GPe
NAC
SEP
CBL
FI
MFG
PrCG
RoG
HiB
HiT
CgGr
MoTg
PTR
SC
SN-RN
LiG
SOG
PaO
SMG
Pons
AnG
ITG
MTG
PRG
STG
TTG
CM
DLG
LP
MD
MG
STH
VL
PDYN-OPRM1
FGF9-FGFR3
AGT-HTR2C
PDYN-OPRK1
LAMA1-GPC1
LAMA1-SDC2
LAMA1-SYJ2B
LAMA1-ITGA3
APOE-GPC4
WNT10B-FZD2
LAMA1-ITGAV
PTHLH-ADCYAP1R1
ARPC5-ADRB2
PDGFB-PDGFRA
GNAI2-ORDZ
GNAI2-OPRK1
PTHLH-ADRB2
LAMA1-CHRM1
IGSF10-MILR1
APOE-GPC5
RGMB-BMPR1B
SLIT1-ROBO1
NCAN-CDH2
SEMA4F-NRP2
PAPLN-SIRPA
PTHLH-PRLHR
ACTR2-ADRB2
NCAN-SDC3
WNT6-FZD2
RSPO3-FZD8
NPY-GPR83
PROS1-AXL
RPS27A-ADRB2
PDGFB-S1PR1
LAMA1-ITGA2
CD24-SIGLEC10
GNAI2-NPY1R
PROS1-MERTK
FAT4-DCHS1
SLIT1-ROBO2
WNT10B-FZD8
CORT-SSTR1
4
2
0
-2
-4
b
Spearman r
0.41
0.35
0.24
0.42
0.34
0.32
0.27
0.27
0.27
0.28
0.40
0.41
0.44
0.34
0.32
0.33
0.47
0.59
0.30
0.25
0.33
0.55
0.57
0.26
0.60
0.34
0.38
0.49
0.40
0.47
0.54
0.28
0.29
0.22
0.27
0.39
0.25
0.44
0.45
0.29
0.65
0.50
0.53
0.60
0.55
0.50
0.45
0.40
0.35
0.30
0.20

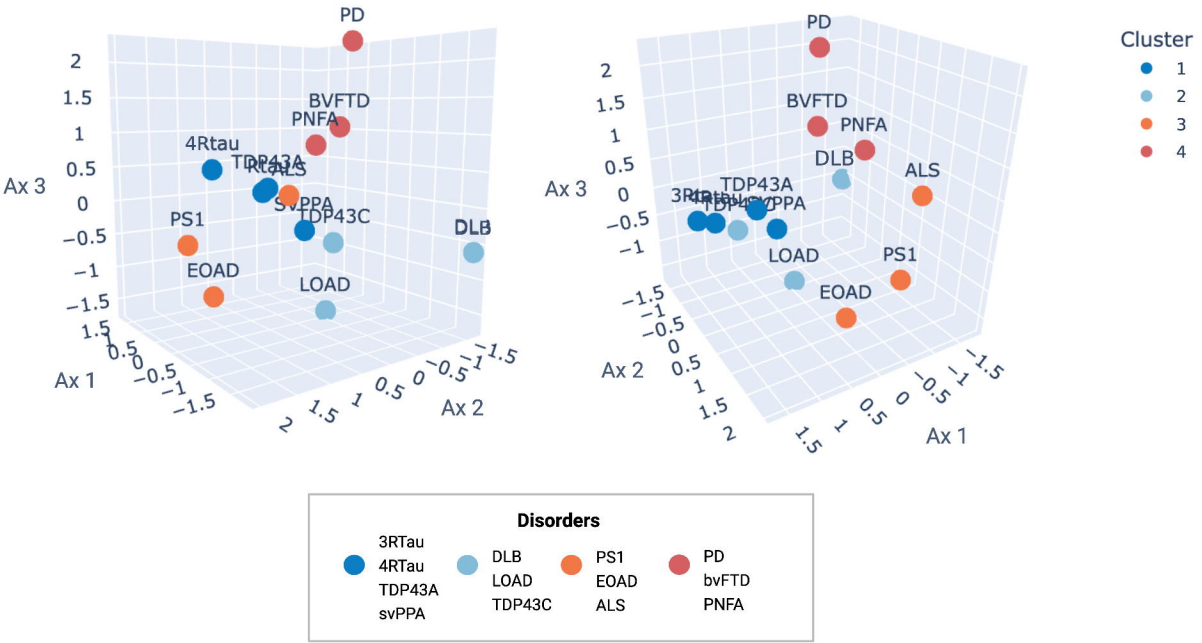
PD
BVFTD
PNFA
4Rtau
TDP43A
3RTau
ALS
svPPA
TDP43C
PS1
DLB
EOAD
LOAD
Ax 3
Ax 1
Ax 2
Cluster
1
2
3
4
Disorders
3RTau
4RTau
TDP43A
svPPA
DLB
LOAD
TDP43C
PS1
EOAD
ALS
PD
bvFTD
PNFA